

 Open access • Posted Content • DOI:10.1101/2020.11.05.369629

Single-molecule analysis reveals cooperative stimulation of Rad51 filament nucleation and growth by mediator proteins — [Source link](#)

[Ondrej Belan](#), [Consuelo Barroso](#), [Artur Kaczmarczyk](#), [Roopesh Anand](#) ...+8 more authors

Institutions: [Francis Crick Institute](#), [Imperial College London](#)

Published on: 05 Nov 2020 - [bioRxiv](#) (Cold Spring Harbor Laboratory)

Topics: [Strand invasion](#), [RAD51](#), [Protein filament](#), [Homologous recombination](#) and [DNA damage](#)

Related papers:

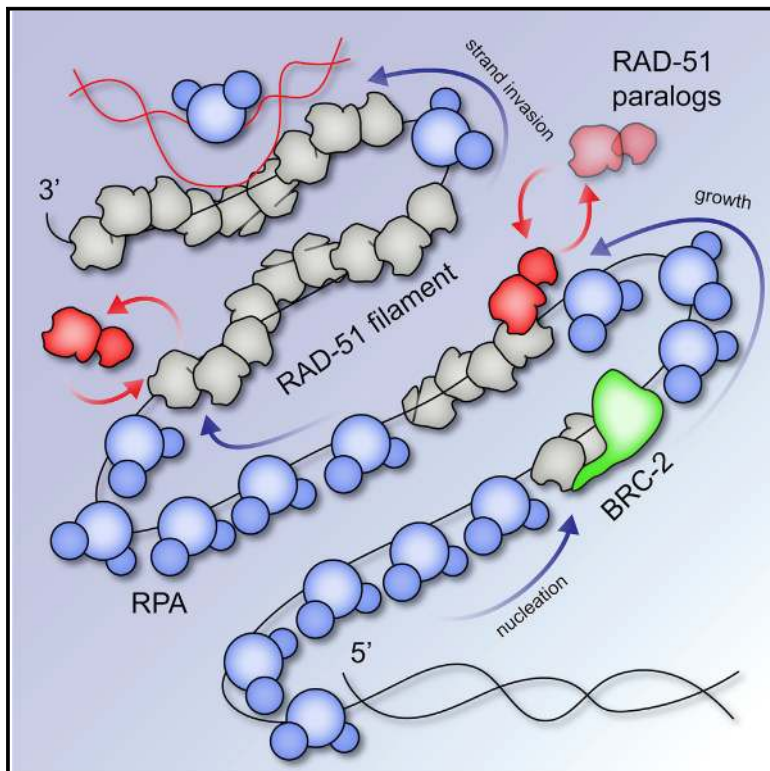
- [Single-molecule analysis reveals cooperative stimulation of Rad51 filament nucleation and growth by mediator proteins.](#)
- [Rad52 oligomeric N-terminal domain stabilizes Rad51 nucleoprotein filaments and contributes to their protection against Srs2](#)
- [CeBRC-2 stimulates D-loop formation by RAD-51 and promotes DNA single-strand annealing.](#)
- [Single-molecule localization microscopy reveals molecular transactions during RAD51 filament assembly at cellular DNA damage sites](#)
- [Human RAD51 paralogue, SWSAP1, fosters RAD51 filament by regulating the anti-recombinase, FIGNL1 AAA+ ATPase](#)

Share this paper:    

View more about this paper here: <https://typeset.io/papers/single-molecule-analysis-reveals-cooperative-stimulation-of-1x34yczhh5>

Single-molecule analysis reveals cooperative stimulation of Rad51 filament nucleation and growth by mediator proteins

Graphical Abstract



Authors

Ondrej Belan, Consuelo Barroso, Artur Kaczmarczyk, ..., Enrique Martinez-Perez, David S. Rueda, Simon J. Boulton

Correspondence

david.rueda@imperial.ac.uk (D.S.R.), simon.boulton@crick.ac.uk (S.J.B.)

In Brief

Belan et al. exploit single-molecule approaches to reveal the mechanism of *C. elegans* Rad51 filament assembly in the presence of recombination mediators. BRCA2 primarily enhances Rad51 nucleation on ssDNA, whereas Rad51 paralogs dynamically engage with 5' Rad51 filament ends and stimulate filament growth in a 3'-5' direction.

Highlights

- *C. elegans* BRCA2 and Rad51 paralogs synergistically promote Rad51 filament assembly
- Rad51 paralogs dynamically engage with the 5' Rad51 filament ends
- Rad51 paralogs stimulate Rad51 filament growth in a 3'-5' direction
- Retention of Rad51 paralogs at filament ends hinders growth and blocks HR *in vivo*



Article

Single-molecule analysis reveals cooperative stimulation of Rad51 filament nucleation and growth by mediator proteins

Ondrej Belan,¹ Consuelo Barroso,² Artur Kaczmarczyk,^{4,5} Roopesh Anand,¹ Stefania Federico,³ Nicola O'Reilly,³ Matthew D. Newton,^{4,5} Erik Maeots,⁶ Radoslav I. Enchev,⁶ Enrique Martinez-Perez,² David S. Rueda,^{4,5,*} and Simon J. Boulton^{1,7,*}

¹DSB Repair Metabolism Laboratory, The Francis Crick Institute, London NW1 1AT, UK

²Meiosis group, MRC-London Institute of Medical Sciences, London W12 0NN, UK

³Peptide Chemistry STP, The Francis Crick Institute, London NW1 1AT, UK

⁴Department of Infectious Disease, Faculty of Medicine, Imperial College London, London W12 0NN, UK

⁵Single Molecule Imaging Group, MRC-London Institute of Medical Sciences, London W12 0NN, UK

⁶Visual Biochemistry Laboratory, The Francis Crick Institute, London NW1 1AT, UK

⁷Lead contact

*Correspondence: david.rueda@imperial.ac.uk (D.S.R.), simon.boulton@crick.ac.uk (S.J.B.)

<https://doi.org/10.1016/j.molcel.2020.12.020>

SUMMARY

Homologous recombination (HR) is an essential DNA double-strand break (DSB) repair mechanism, which is frequently inactivated in cancer. During HR, RAD51 forms nucleoprotein filaments on RPA-coated, resected DNA and catalyzes strand invasion into homologous duplex DNA. How RAD51 displaces RPA and assembles into long HR-proficient filaments remains uncertain. Here, we employed single-molecule imaging to investigate the mechanism of nematode RAD-51 filament growth in the presence of BRC-2 (BRCA2) and RAD-51 paralogs, RFS-1/RIP-1. BRC-2 nucleates RAD-51 on RPA-coated DNA, whereas RFS-1/RIP-1 acts as a “chaperone” to promote 3' to 5' filament growth via highly dynamic engagement with 5' filament ends. Inhibiting ATPase or mutation in the RFS-1 Walker box leads to RFS-1/RIP-1 retention on RAD-51 filaments and hinders growth. The *rfs-1* Walker box mutants display sensitivity to DNA damage and accumulate RAD-51 complexes non-functional for HR *in vivo*. Our work reveals the mechanism of RAD-51 nucleation and filament growth in the presence of recombination mediators.

INTRODUCTION

Homologous recombination (HR) is a largely error-free mechanism of DNA double-strand break (DSB) repair. DSBs can arise spontaneously because of replication fork stalling or collapse or after exposure to DNA-damaging agents, such as ionizing radiation. HR repair is also essential to produce inter-homolog crossovers necessary for correct chromosome segregation at the first meiotic division (Chapman et al., 2012).

HR is a complex process comprising several conserved steps. First, broken double-stranded DNA (dsDNA) ends are nucleolytically processed, yielding 2–4 kb of single-stranded DNA (ssDNA) coated by replication protein A (RPA). RPA is displaced by Rad51, a eukaryotic recombinase that forms helical nucleoprotein filaments with single-stranded DNA (ssDNA). Within the filament, DNA is extended 1.5-fold over the dsDNA contour length, with a stoichiometry of 3 nt per RAD51 monomer and six RAD51 monomers per helical turn (Xu et al., 2017). Rad51 filaments then search for a homologous DNA sequence within sister chromatids

or homologous chromosomes, followed by strand invasion and displacement loop (D-loop) intermediate formation. The invading 3' DNA end is extended by polymerases and processed by multiple redundant pathways to complete the repair and to restore the broken DNA strand (Chapman et al., 2012).

Given the lower affinity of Rad51 for ssDNA, compared with RPA, mediator proteins that promote RPA displacement are crucial for efficient HR. In higher eukaryotes, BRCA2 and Rad51 paralogs (RAD51B, RAD51C, RAD51D, XRCC2, and XRCC3 in human cells) are among the most critical mediator proteins. Loss of BRCA2 or individual RAD51 paralogs results in sensitivity to DSB-inducing agents, loss of Rad51 foci at sites of DSBs and defective HR repair (Chapman et al., 2012). Mutations in BRCA2 or Rad51 paralogs confer hereditary breast, ovarian, and other cancers (King et al., 2003; Loveday et al., 2011; Meindl et al., 2010).

Biochemical studies have shown that sub-stoichiometric amounts of full-length human BRCA2 promote nucleation of RAD51 on ssDNA and enhance its strand-exchange activity in



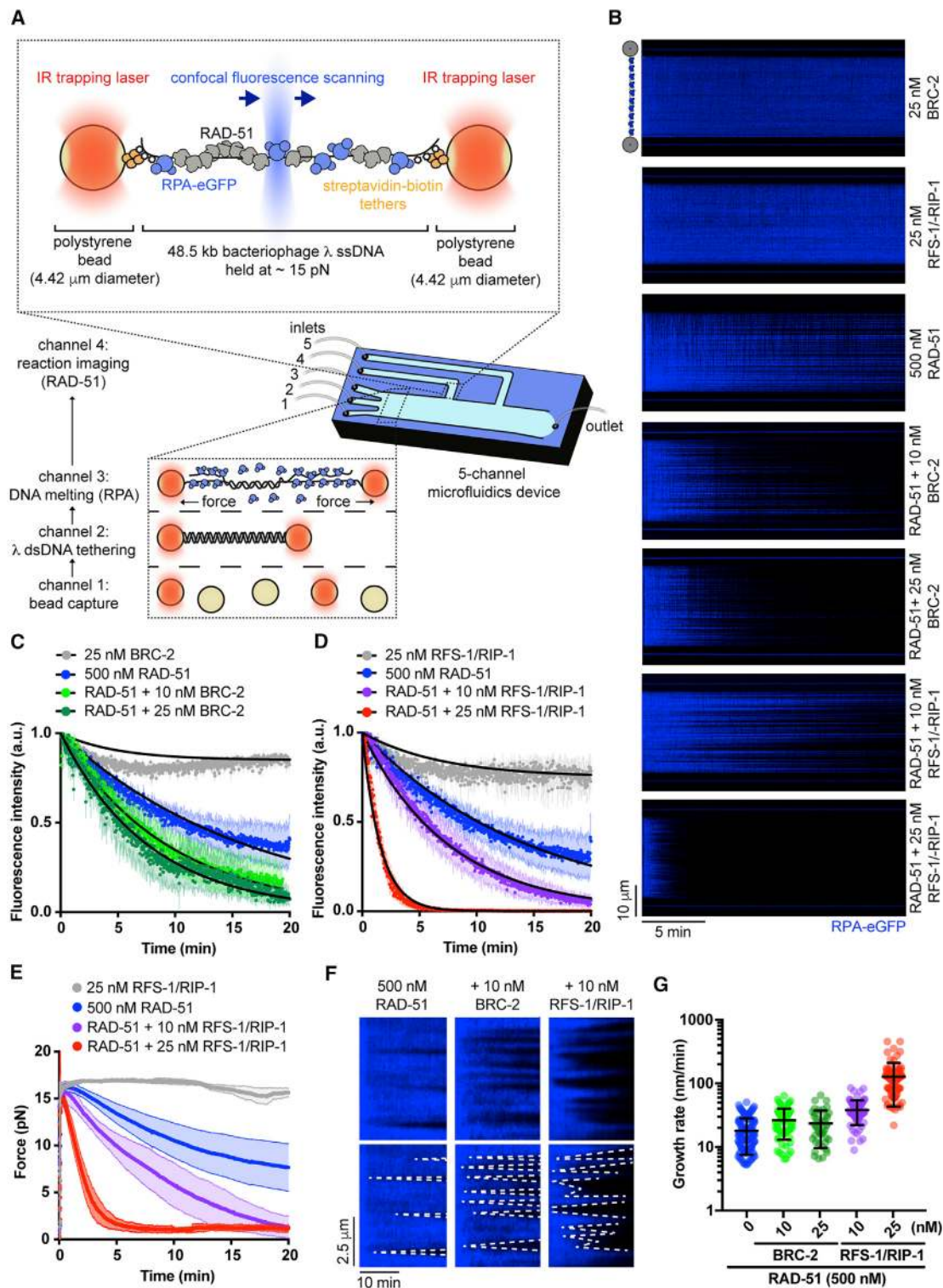


Figure 1. BRC-2 and RFS-1/RIP-1 display differential roles in RAD-51 filament assembly and growth on RPA-coated ssDNA

(A) Schematic of the experimental C-trap set-up.

(B) Kymograph showing the displacement of RPA-eGFP by 500 nM RAD-51 in the presence or absence of BRC-2 or RFS-1/RIP-1.

(C) Normalized fluorescence intensity for RPA-eGFP signal over time in the presence of RAD-51 and indicated amounts of BRC-2; shaded area represents SEM ($n = 3\text{--}8$ molecules). Black lines represent exponential fits.

(legend continued on next page)

bulk assays (Jensen et al., 2010; Liu et al., 2010; Thorslund et al., 2010). BRCA2 also binds RAD51-ssDNA filaments and inhibits Rad51 ATPase activity, thereby suppressing Rad51 release from DNA (Petalcorin et al., 2007; Jensen et al., 2010). Although nematode Rad51 paralogs (RFS-1/RIP-1) do not bind to free RAD-51 in solution, they can bind to and stabilize Rad51 filaments (Taylor et al., 2015). Furthermore, bulk studies have shown that the DNA strand-exchange activity of Rad51 is stimulated by the addition of sub-stoichiometric amounts of human RAD51B-RAD51C (Sigurdsson et al., 2001) or the nematode Rad51 paralog complex (Taylor et al., 2015). Rad51 paralogs have been suggested to intercalate into Rad51 filaments and serve as roadblocks to prevent filament disassembly by anti-recombinases, such as Srs2 (Liu et al., 2011).

Although current evidence implicates BRCA2 and Rad51 paralogs in positively regulating Rad51 function, an understanding of their dynamics during the HR reaction remains unclear. Single-molecule studies of the *E. coli* RecA recombinase have revealed that nucleoprotein filaments rapidly form in the presence of bacterial single-stranded binding protein (SSB) by a two-step mechanism: rate-limiting nucleation, followed by rapid, bi-directional filament growth with a 2-fold kinetic preference for the 5' → 3' direction along an ssDNA backbone (Bell et al., 2012; Galletto et al., 2006). In contrast, human Rad51 filaments formed in the presence of RPA *in vitro* are rare and grow very slowly (Candelli et al., 2014; Hilario et al., 2009). Currently, the mechanisms that promote presynaptic Rad51 filament assembly in eukaryotes remain unknown.

Here, we report a single-molecule system to monitor the real-time dynamics of nematode RAD-51-ssDNA filament assembly and how that is modulated by the recombination mediators BRC-2 and RFS-1/RIP-1. Through a combination of microfluidics, optical tweezers, and fluorescence microscopy, we show that BRC-2 acts primarily as a RAD-51 nucleation factor on RPA-coated ssDNA, whereas RFS-1/RIP-1 acts on nucleated RAD51-ssDNA complexes to stimulate filament growth. Direct real-time imaging of RFS-1/RIP-1 also revealed an unexpected and highly dynamic engagement with the 5' RAD-51 filament ends, which requires ATP turnover by RFS-1. Transient RFS-1/RIP-1 binding to the nascent 5' RAD-51 filament end prevents dissociation of RAD-51 protomers and stimulates filament growth in a 3' → 5' direction. However, blocking ATPase or mutation of the RFS-1 Walker A box increases the dwell-time of RFS-1/RIP-1 on the RAD-51 filament ends, which stabilizes RAD-51 on DNA, but inhibits filament growth and strand-exchange activity (Taylor et al., 2015). Finally, unlike nematode strains lacking *rfs-1*, which are sensitive to DNA damage and fail to form RAD-51 foci, *rfs-1* Walker box mutants accumulate non-functional RAD-51 foci, which form in a BRC-2-dependent manner. We propose that distinct mechanisms of the two mediator proteins act sequentially to synergistically promote efficient RAD-51 nucleation, filament growth, and HR stimulation.

RESULTS

Differential action of mediator proteins on RAD-51 presynaptic complex assembly

To examine how recombination mediators affect the nucleation and/or growth of Rad51 filaments in the presence of its physiological competitor RPA, we have reconstituted RAD-51 filament assembly at a single-molecule level using fluorescently labeled *C. elegans* proteins and a combination of optical tweezers, confocal fluorescence microscopy, and microfluidics (C-trap set-up; Figure 1A) (Gutierrez-Escribano et al., 2019; Newton et al., 2019). To generate an HR substrate, 48.5-kb doubly biotinylated bacteriophage λ dsDNA was trapped between two polystyrene streptavidin-coated beads, force-melted *in situ* to produce ssDNA (Candelli et al., 2013) (Figure S1A), and then coated with RPA-eGFP fusion protein (Figure 1A). The RAD-51 assembly was initiated by moving the traps to protein channels containing RAD-51 and/or mediator proteins (Figure 1A) in the presence of ATP. RAD-51 assembly and RPA-eGFP displacement was monitored by loss of eGFP fluorescence and simultaneous decrease in the force exerted on ssDNA that accompanies recombinase filament formation (Hegner et al., 1999).

To characterize the role of mediator proteins in our system, we performed RPA-eGFP displacement experiments with RAD-51 in the presence or absence of his₆-MBP-BRC-2 (hereafter referred to as BRC-2), a recombination mediator and ortholog of the breast and ovarian cancer tumor-suppressor protein, BRCA2 (Martin et al., 2005; Petalcorin et al., 2007; Petalcorin et al., 2006) (Figure 1B). Although RAD-51 alone slowly assembles on RPA-coated ssDNA in the presence of ATP (half-time of 10.16 ± 0.8 min, 95% CI), the addition of sub-stoichiometric concentrations of BRC-2 stimulates the overall assembly rate, reducing assembly half-time to 5.3 ± 0.3 min (95% CI; Figure 1C). We next performed RPA-eGFP displacement assays with RAD-51 in the presence of the RFS-1/RIP-1-3xFLAG (hereafter referred to as RFS-1/RIP-1) complex. Addition of sub-stoichiometric concentrations of RFS-1/RIP-1 greatly stimulates the RAD-51 filament assembly rate, reducing assembly half-time from ~ 10 min to ~ 1 min (Figures 1B and 1D). This is accompanied by a decrease in force measured between the optical traps from ~ 15 pN to ~ 1 pN (Figure 1E), which is in agreement with increased stiffness of RAD-51-coated ssDNA (Hegner et al., 1999). Consistent with its weak ssDNA affinity (Taylor et al., 2015), RFS-1/RIP-1 did not induce any detectable RPA displacement on its own (Figures 1B, 1D, and 1E).

In addition to estimating overall assembly rate, this approach allowed us to resolve individual growing RAD-51 nuclei and measure growth rates of RAD-51 filaments (Figures 1F and 1G). It should be noted that, under these conditions, multiple nucleation events within a dark pixel can occur. However, those events are unlikely, would average out during data analysis, and would not affect the overall conclusion. We confirmed that RAD-51 grows

(D) Normalized fluorescence intensity for RPA-eGFP signal over time in the presence of RAD-51 and indicated amounts of RFS-1/RIP-1; shaded area represents SEM ($n = 3-6$ molecules). Black lines represent exponential fits.

(E) Force measured between the traps as a function of time in indicated RFS-1/RIP-1 concentrations; shaded area represents SEM ($n = 3-8$ molecules).

(F) Examples of individual growing RAD-51 filaments (dark). Growth rate was measured as a slope of the border of RPA-eGFP displaced signal.

(G) Quantification of growth rates in indicated conditions.

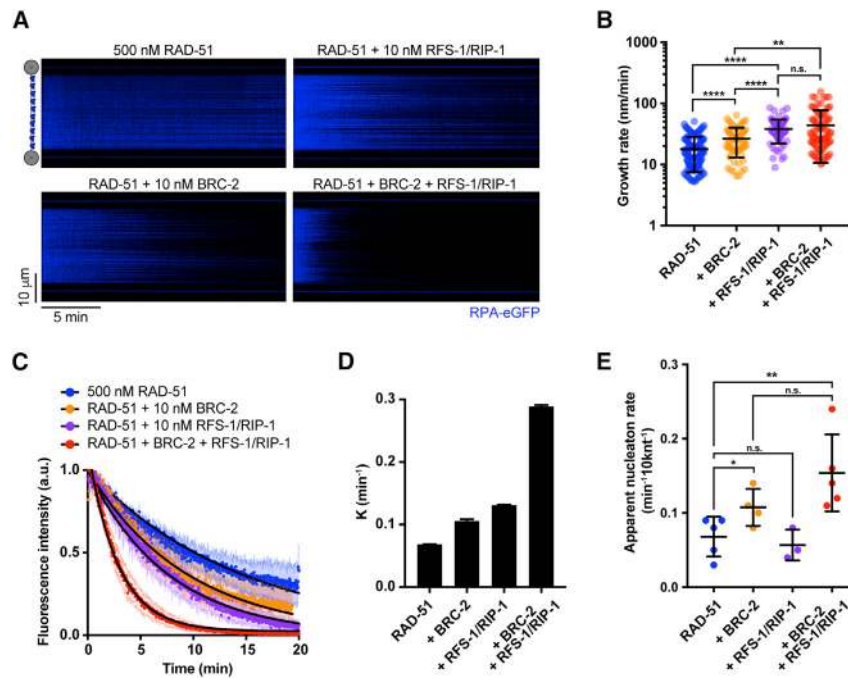


Figure 2. BRC-2 and RFS-1/RIP-1 synergize to ensure efficient RAD-51 filament assembly

(A) Kymograph showing the displacement of RPA-eGFP by 500 nM RAD-51 in the presence or absence of BRC-2 and/or RFS-1/RIP-1.

(B) Quantification of growth rates in indicated conditions. Error bars represent SD. $p > 0.05$ (n.s.), $*p \leq 0.05$, $**p \leq 0.01$, $***p \leq 0.001$, $****p \leq 0.0001$. Mann-Whitney test.

(C) Normalized fluorescence intensity for RPA-eGFP signal in the presence or absence of BRC-2 and/or RFS-1/RIP-1; shaded area represents SEM ($n = 4-8$ molecules). Black lines represent exponential fits.

(D) K_{off} values for RPA-eGFP displacement traces calculated from exponential fits to the data in (C); error bars represent upper and lower K value limits.

(E) Quantification of apparent nucleation frequencies in indicated conditions. Error bars represent SD. $p > 0.05$ (n.s.), $*p \leq 0.05$, $**p \leq 0.01$. Mann-Whitney test.

slowly (mean, 17.9 ± 1.8 nm/min, 95% CI; which corresponds roughly to 38.6 ± 3.9 nt/min; 500 nM protein) compared with bacterial RecA (~ 40 nm/min under similar conditions (Bell et al., 2012)). RFS-1/RIP-1 strongly stimulates growth rates of individual RAD-51 nuclei (mean, 38.1 ± 4.0 nm/min, 95% CI; which corresponds to 82.1 ± 8.6 nt/min; 10 nM RFS-1/RIP-1; Figures 1F and 1G). Notably, BRC-2 had a significant, albeit modest, effect on RAD-51 growth when compared with RFS-1/RIP-1 (mean of 26.4 ± 3.2 nm/min, 95% CI; which corresponds to 56.9 ± 6.9 nt/min; 10 nM BRC-2). Our data suggest that BRC-2 acts primarily as a RAD-51 nucleation factor (Shahid et al., 2014), whereas RFS-1/RIP-1 acts primarily as a RAD-51 filament growth factor on RPA-coated ssDNA.

BRC-2 and RFS-1/RIP-1 synergize to ensure efficient RAD-51 presynaptic filament assembly

These distinct modes of action raised the possibility that the mediator proteins may cooperate to enhance RAD-51 filament assembly when combined in a single reaction. Inclusion of both proteins in the reaction (Figure 2A), results in increased growth rate of individual RAD-51 filaments (mean, 43.8 ± 7.0 nm/min, 95% CI; which corresponds to 94.4 ± 15.1 nt/min; 10 nM BRC-2, 10 nM RFS-1/RIP-1), which was not significantly different from the RAD-51 filament growth rates measured in the presence of RFS-1/RIP-1 only (Figures 2A and 2B). These results indicate that RFS-1/RIP-1 and BRC-2 do not synergize to promote RAD-51 filament growth, but rather, that RFS-1/RIP-1 is the major filament growth stimulatory factor in the combined assembly reaction. However, when combined, BRC-2 and RFS-1/RIP-1 display a synergistic effect on overall RAD-51 assembly rates on RPA-coated ssDNA (Figures 2A and 2C), strongly reducing overall assembly half-time to 2.4 min (95% CI) and increasing the overall assembly rate to 0.29 min^{-1} in contrast

confirmed assembly kinetics obtained from fluorescence-intensity quantification (Figure S1B). To explore whether the observed synergy stems from BRC-2 acting as a nucleation factor and RFS-1/RIP-1 promoting growth of individual RAD-51 nuclei, we analyzed RPA-eGFP displacement traces using a custom-written algorithm to extract apparent RAD-51 nucleation rates on individual λ ssDNA molecules (Figure S1C). We observed increased nucleation rates only in the presence of BRC-2, not RFS-1/RIP-1 (Figure 2E). Taken together, these results further strengthen the notion that BRC-2 primarily nucleates RAD-51 on RPA-coated ssDNA, which is then extended into nascent filaments by RFS-1/RIP-1 stimulation.

RFS-1/RIP-1 promotes filament growth in the 3' to 5' direction

Using bulk fluorescence to estimate kinetics of protein binding and dissociation from short Cy3-labeled oligonucleotides, we have previously observed that RFS-1/RIP-1 binds and stabilizes the 5' end of pre-assembled RAD-51 filaments (Taylor et al., 2016). In contrast, we did not detect any stabilization effect at the 3'-filament end. Given this previously described polarity and that RPA-eGFP displacement slopes appear specifically steeper in one direction in kymographs in the presence of RFS-1/RIP-1 compared with the conditions in which RFS-1/RIP-1 was absent (Figure 1F), we reasoned that growth stimulation promoted by RFS-1/RIP-1 might lead to preferential protomer addition at only one end of RAD-51 filaments.

To examine the polarity of filament growth, we developed a protocol to generate an asymmetrically positioned ssDNA gap of defined length on λ DNA using Cas9 nickase and DNA melting *in situ* (Figures 3A and S2A). We confirmed the position of the ssDNA gap using eGFP-RPA fluorescence to mark the ssDNA portion of the gapped molecule (Figures 3B and 3C). We then

to 0.07 min^{-1} in the absence of recombination mediators or 0.1 and 0.13 min^{-1} in the presence of BRC-2 or RFS-1/RIP-1 (Figure 2D). Force measurements

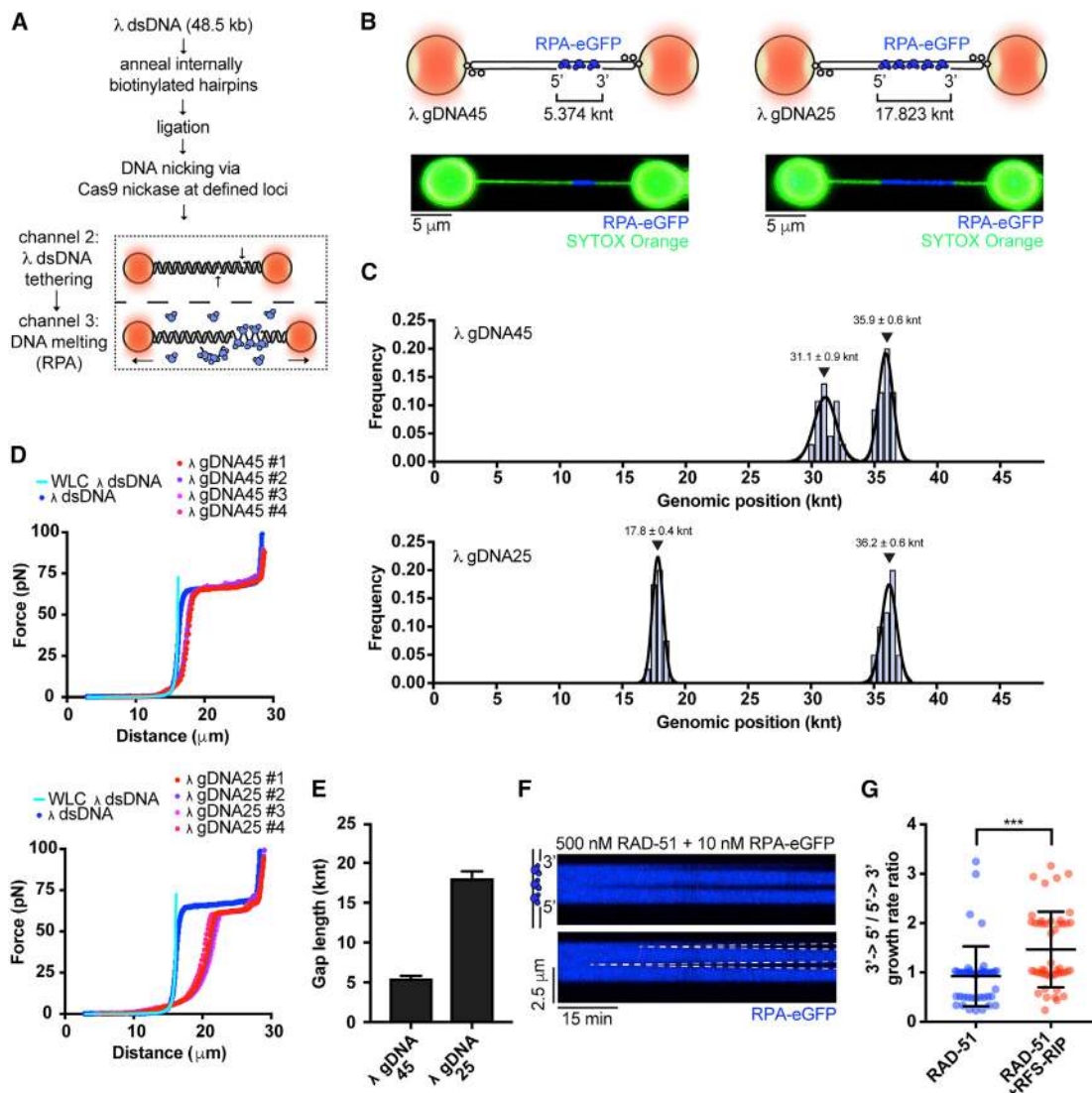


Figure 3. RFS-1/RIP-1 promotes filament growth in the 3' to 5' direction

(A) Schematic of protocol designed to generate gapped λ DNA (gDNA) substrates.

(B) Schematic of the two λ gDNA substrates employed to investigate RAD-51 filament growth polarity. Representative image of asymmetrically positioned RPA-eGFP coated 5-k nt (λ gDNA45) and 17-k nt (λ gDNA25) ssDNA gap within λ DNA held at 15 pN force. dsDNA stained by 50 nM SYTOX orange.

(C) Genomic position analysis of the ssDNA gap evaluated from RPA-eGFP signal boundaries; 20–32 scans analyzed per each histogram. Black lines represent Gaussian fits. Error bars represent SD

(D) Force-extension curves of λ dsDNA (blue) and multiple λ gDNA45 or λ gDNA25 molecules. Light blue line represents worm-like chain model (WLC) fit for 48.5-kb-long dsDNA.

(E) ssDNA gap length of λ gDNA45 and λ gDNA25 calculated from WLC model fits to traces presented in (D). Error bars represents SD.

(F) Examples of individual growing RAD-51 filaments (dark) on gapped DNA construct. Growth rate was measured as a slope of the border of RPA-eGFP displaced signal.

(G) Quantification of growth rate polarity of 500 nM RAD-51 in the presence or absence of 10 nM RFS-1/RIP-1.

force-stretched individual gapped DNA molecules to compare them to λ dsDNA (Figure 3D). To calculate the apparent contour length of these molecules, we applied a worm-like chain fitting to individual force-extension curves. From relative contour length increases, we were able to calculate the length of ssDNA within the substrate (Figure 3E). These are in agreement with the predicted ssDNA gap length. To suppress extensive RAD-51

nucleation and better resolve individual RAD-51 filaments, free RPA-eGFP was added to the imaging channel. This setup allowed us to accurately assess directionality of RAD-51 filament growth. Surprisingly, unlike RecA, which grows preferentially in a 5' \rightarrow 3' direction, nematode RAD-51 displays mostly symmetric growth with only a slight bias toward the 5' \rightarrow 3' direction (Figures 3F and S2B). Addition of RFS-1/RIP-1 resulted in a 2-fold

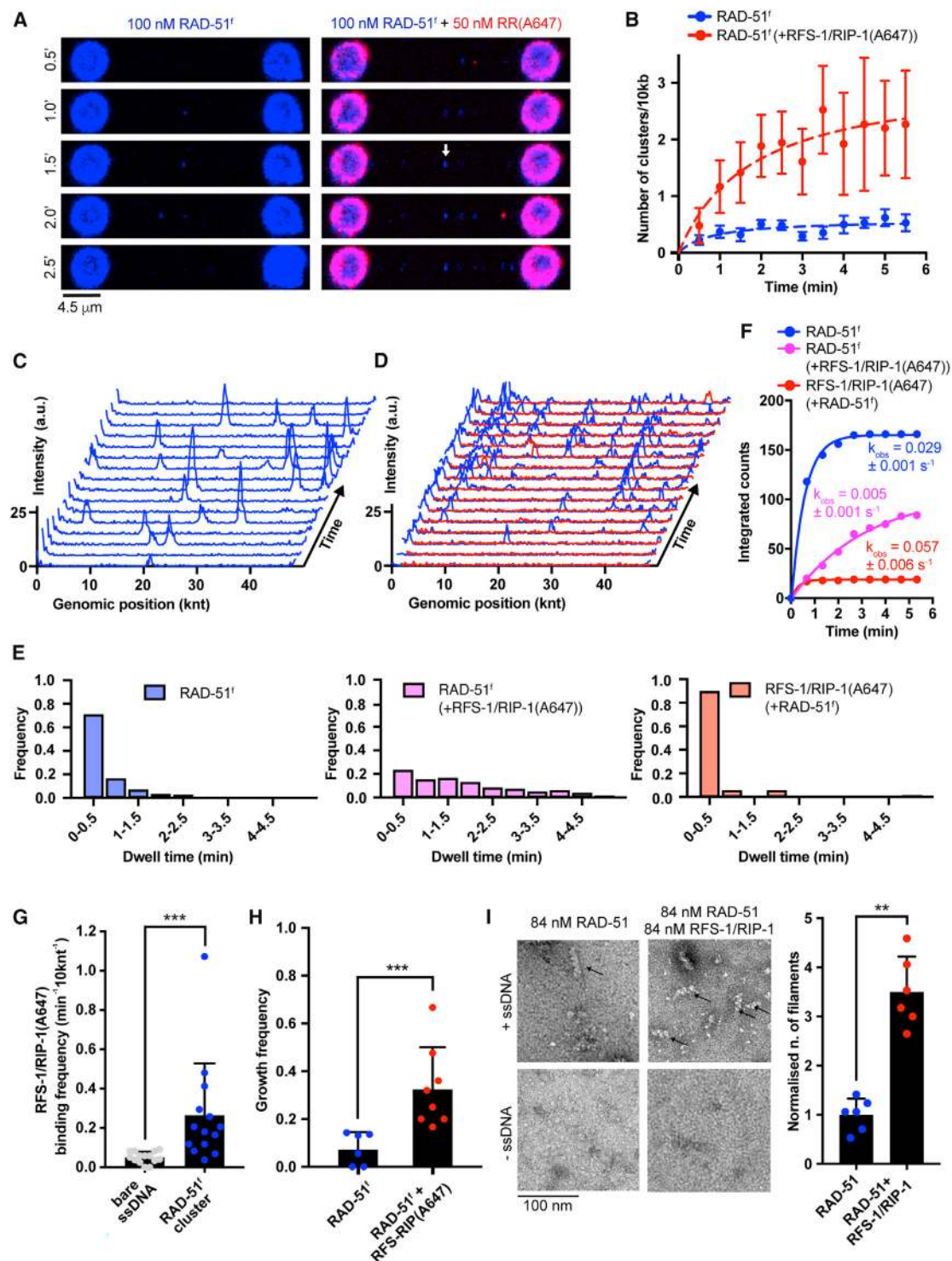


Figure 4. Highly dynamic RFS-1/RIP-1 complex “chaperones” DNA-bound RAD-51 clusters by preventing RAD-51 dissociation
 (A) Fluorescence images taken after subsequent RAD-51^f or RAD-51^f+RFS-1/RIP-1(A647) incubation-detection cycles with the same ssDNA (no RPA) construct; cumulative incubation time (min) is indicated. Scale bar, 4.5 μm. Arrow indicates a growth event. RAD-51^f signal shown in blue. RFS-1/RIP-1(A647) signal shown in red.
 (B) Quantification of RAD-51^f nucleation frequency over time in the presence (n = 9 molecules) or absence (n = 11 molecules) of RFS-1/RIP-1(A647). Exponential fits are displayed. Error bars represent SEM.

(legend continued on next page)

stimulation of the 3' → 5' growth rates, resulting in net growth from the 5'-filament end (Figures 3G and S2B). These results indicate that RFS-1/RIP-1-mediated growth stimulation of RAD-51 filaments is asymmetric and occurs at 5'-filament ends.

RFS-1/RIP-1 acts as a molecular chaperone to stabilize RAD-51

Rad51/RecA-ssDNA filaments are in a state of dynamic equilibrium, where they grow and shrink exclusively from filament ends (Joo et al., 2006; van Mameren et al., 2009). Previous work established that human Rad51-dsDNA filaments dissociate from the ends in bursts of multiple protomers interspersed by pauses (van Mameren et al., 2009). Similar behavior was later observed for Rad51-ssDNA complexes (Candelli, 2013). In contrast, growth of RecA (Bell et al., 2012) and Rad51 (Candelli et al., 2014) filaments occurs predominantly by rate-limiting slow addition of monomers. Given the resolution of our setup, we were not able to accurately monitor RAD51 protomer association and dissociation events from filament ends. To circumvent that issue, we employed a previously described reverse setup (Candelli et al., 2014), in which low concentrations of labeled protein are used to obtain sparse nucleation events containing only a few RAD-51 protomers. Single-step photobleaching calibration was used to quantify the number of fluorophores present in each cluster. Given that recombinase filaments can grow and dissociate only from filament ends (Joo et al., 2006; van Mameren et al., 2009), this system allows us to assess growth and dissociation dynamics of small RAD-51 clusters and use that as a proxy for events occurring at the ends of long ssDNA RAD-51 filaments.

To investigate the molecular mechanism of RFS-1/RIP-1-mediated RAD-51 filament growth stimulation at a single-protomer level, we stoichiometrically labeled RAD-51 with fluorescein (6-FAM) (Amitani et al., 2010) (referred to as RAD-51^f; Figure S3A), which retained wild-type (WT) levels of DNA binding (Figure S3B) and D-loop formation activity (Figure S3C). To ensure RAD-51^f displaces RPA as efficiently as unlabelled RAD-51, we monitored assembly of RAD-51^f on RPA-mCherry-coated ssDNA (Figure S3D). Because of the fluorescence bleed through between the channels, we were unable to monitor RPA-mCherry displacement by fluorescence decrease. We, therefore, monitored the force change associated with RAD-51 filament

formation on ssDNA. The force decreased to a similar extent in the presence of either RAD-51^f or unlabelled RAD-51. To visualize individual fluorescently labeled RAD-51^f clusters (a DNA-bound species containing one or more RAD-51^f protomers), we employed a “dipping protocol” (Figure S4A), where λ ssDNA trapped between two beads is incubated for a defined period of time in a channel containing RAD-51^f. ssDNA bound by RAD-51^f is subsequently moved to a protein-free observation channel and visualized by fluorescence microscopy. Repeated incubation-detection cycles allow for kinetic analysis of RAD-51^f nucleation and growth. Consistent with previous literature (Brouwer et al., 2018; Candelli et al., 2014), RAD-51 binding to ssDNA is not affected by the force at which ssDNA is held (Figure S4B). Thus, we proceeded with 15 pN force regime. Nucleation frequency of RAD-51^f clusters (k_{obs}) assessed after a single round of dipping in the presence of ATP displays power dependence with respect to RAD-51^f concentration, according to $k_{\text{obs}} = J [\text{RAD-51}]^n$, in which J is a rate constant and n is the number of protomers in a minimal nucleation unit. In agreement with studies of bacterial RecA ($n = 1.5$ in ATP and $n = 2.2$ in ATP- γ -S) (Bell et al., 2012) and human RAD51 ($n = 1.5$; [Candelli et al., 2014], $n = 1.6 \pm 0.2$ for *C. elegans* RAD-51) (Figures S4C and S4D), indicating that RAD-51^f nucleates as a small species on ssDNA, most likely a dimer or a monomer. Consistent with our previous result (Figures 1B and 1C), inclusion of BRC-2 increased nucleation frequencies in the presence of RPA in this assay (Figure S4D). Addition of unlabeled RFS-1/RIP-1 also increased RAD-51 nucleation rates, albeit to a lesser extent than in the presence of BRC-2.

To examine the dynamics of RFS-1/RIP-1 during RAD-51 filament assembly, we fused the C terminus of RIP-1 to a ybbr tag (Yin et al., 2006) and labeled the corresponding complex with Alexa 647 dye (referred to as RFS-1/RIP-1(A647); Figures S5A and S5B). RFS-1/RIP-1(A647) retains its ability to bind RAD-51 filaments (Figure S5C) and stimulate strand exchange (Figure S5D). Time-resolved experiments revealed a significant accumulation of RAD-51^f clusters over time in the presence of RFS-1/RIP-1(A647) and ATP (Figures 4A and 4B). Without RFS-1/RIP-1(A647), RAD-51^f clusters are highly dynamic. They bind and dissociate rapidly from ssDNA (Figure 4C). To estimate off-rates of RAD-51^f, we measured dwell-times of individual RAD-51^f clusters. These were calculated from the number of consecutive 30-s

(C) Representative histogram of time-binned intensity versus genomic position on λ DNA for RAD-51^f signal (blue) in the absence of RFS-1/RIP-1(A647). Each line represents 30-s time point.

(D) Representative histogram of time-binned intensity versus genomic position on λ DNA for RAD-51^f signal (blue) in the presence of RFS-1/RIP-1(A647) (red). Each line represents 30-s time point.

(E) Histograms of dwell times of RAD-51^f in the absence (left panel) or presence of RFS-1/RIP-1(A647) (middle panel) or dwell times of RFS-1/RIP-1(A647) in the presence of RAD-51^f (right panel). Lines represent exponential fits. (Top panel: RAD-51^f, $\tau \sim 21.12$ s, $R^2 = 0.99$, $n = 167$ clusters; middle panel: RAD-51^f + RFS-1/RIP-1(A647), $\tau \sim 150.6$ s, $R^2 = 0.95$, $n = 87$ clusters; bottom panel: RFS-1/RIP-1(A647), $\tau \sim 10.28$, $R^2 = 0.99$, $n = 19$ clusters)

(F) Cumulative survival plots of data presented in Figure 2E. Lines represent exponential fits.

(G) Quantification of the frequency of RFS-1/RIP-1(A647) binding to ssDNA and RAD-51 clusters. Individual DNA molecules were analyzed, and the fraction of RFS-1/RIP-1(A647) bound to ssDNA or RAD-51^f cluster was calculated. Data points presented in the panel were pooled from both ATP and ATP- γ -S datasets. Each data point represents one ssDNA molecule analyzed. $p = 0.005$. Wilcoxon test.

(H) Growth frequencies of RAD-51^f clusters (fraction of clusters on a given ssDNA molecule displaying at least one growth event—defined by an increase of protomer number by a minimum of 1—in the presence or absence of RFS-1/RIP-1. $p = 0.0003$. Mann-Whitney test.

(I) Negative stain electron microscopy of RAD-51 filaments formed after 5 min at 25°C in the presence or absence of 250 nM (in nucleotides) 150-mer ssDNA. Black arrows point at RAD-51 filaments. Quantification represents normalized fold increase of number of RAD-51 filaments relative to “RAD-51 + ssDNA only” condition. Six fields of view across different sections of the EM grid were evaluated and plotted. $p = 0.0022$. Mann-Whitney test.

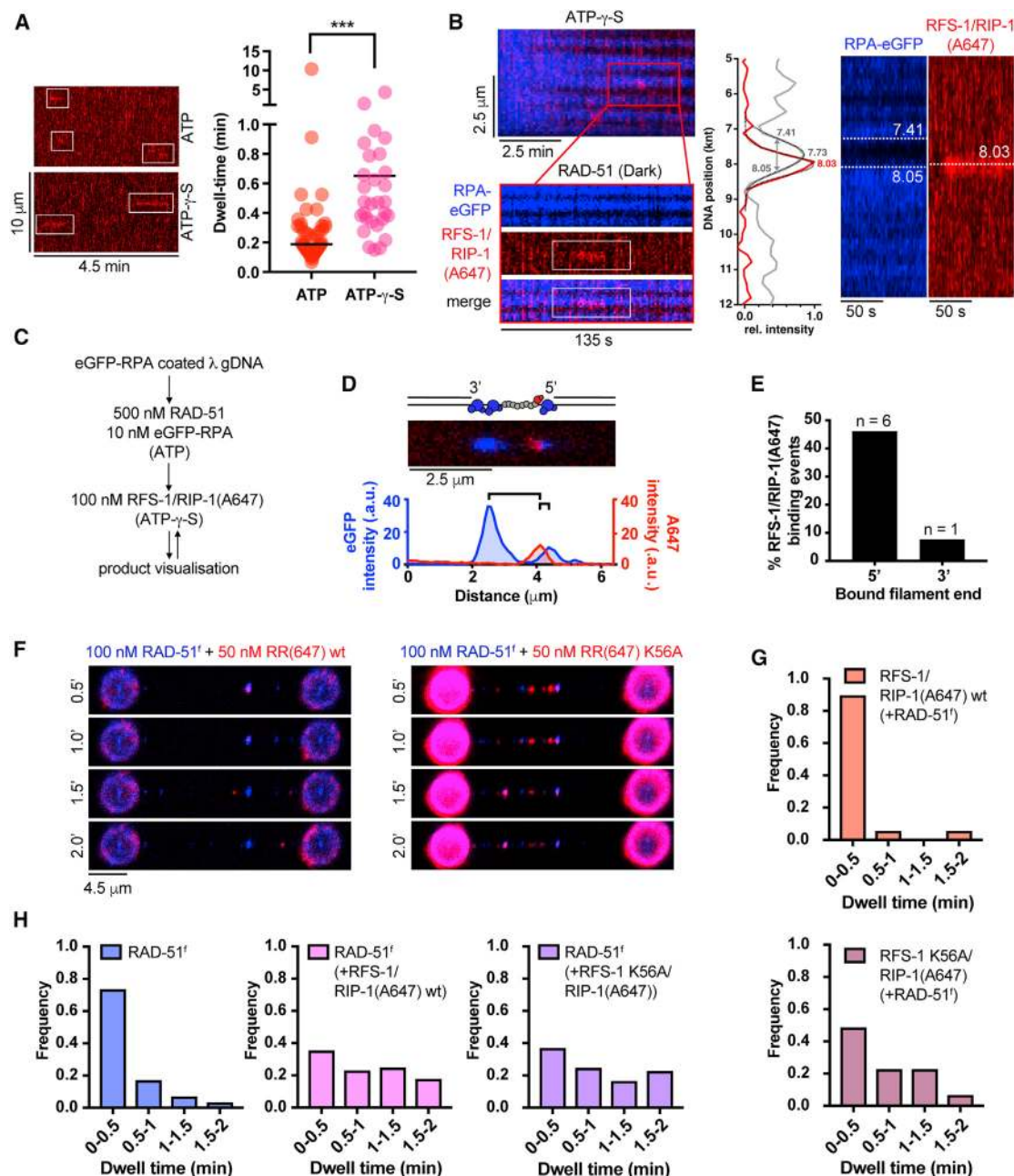


Figure 5. Transient engagement of RFS-1/RIP-1 with the 5' filament ends is mediated by ATPase activity

(A) Representative kymographs of dwelling single RFS-1/RIP-1(A647) (2.5 nM) complexes on RPA-eGFP coated ssDNA in the presence of 500 nM RAD-51 and ATP or ATP- γ -S (left panel). Quantification of experiment shown in left panel, for ATP ($n = 47$ binding events) and ATP- γ -S ($n = 29$ binding events). Black line represents median. $p < 0.0001$. Mann-Whitney test (right panel).

(B) Representative traces of single RFS-1/RIP-1(A647) complexes binding to RAD-51 filaments in ATP- γ -S. RPA-eGFP shown in blue, RAD-51 dark, RFS-1/RIP-1(A647) red. Quantification of the RFS-1/RIP-1(A647) end binding using custom position analysis algorithm. 2D scan showing RFS-1/RIP-1(A647) (red channel) binding to the RAD-51 filament (dark, blue channel) in the presence of RPA-eGFP (blue channel). To obtain the exact location of the RAD-51 paralog with respect to the RAD-51 filament, the center of the filament is resolved first by fitting the reversed eGFP intensity (gray peak). Grey arrow, representing the peak's width, marks the filament's edges. Gaussian fit of the RFS-1/RIP-1(A647) intensity (red peak, red channel) indicates that the paralog binds to the periphery of the RAD-51 filament.

(C) Protocol designed to visualize RFS-1/RIP-1(A647) binding to RAD-51 filaments grown on gapped λ DNA.

(D) 2D scan of representative RAD-51-DNA complex obtained using protocol described in (C). Proximity of A647 signal maximum to eGFP signal maximum on either 3' or 5' RAD-51 filament border was used to estimate the 3' or 5' filament end binding polarity.

(legend continued on next page)

frames in which a detectable FAM signal was present at the same genomic position (Figure 4C). The analysis confirmed RAD-51^f clusters bind to ssDNA with short dwell-times (Figures 4E and 4F). These observations are reminiscent of burst-like dissociation events reported previously at human Rad51 filament ends (van Mameren et al., 2009). Strikingly, inclusion of RFS-1/RIP-1(A647) in the reaction results in a significant increase in the dwell-times of RAD-51^f clusters on ssDNA indicating a stabilization effect mediated by RFS-1/RIP-1 (Figures 4D–4F).

Unexpectedly, direct visualization of RFS-1/RIP-1(A647) molecules revealed that they bind to RAD-51^f clusters with extremely short dwell times (Figures 4E and 4F). Colocalization of RFS-1/RIP-1(A647) with RAD-51^f clusters (Figure 4G) is consistent with recognition of nascent RAD-51 filaments, rather than ssDNA. Collectively, our data indicate that RFS-1/RIP-1 promotes assembly of RAD-51 filaments by shutting down disassembly events at filament ends without being a stable component of DNA-bound RAD-51^f clusters. Hence, RFS-1/RIP-1 acts in a transient manner as a dynamic RAD-51 filament chaperone.

Rapid photobleaching and step-finding analysis (Autour et al., 2018; Watkins and Yang, 2005) allowed us to calibrate the imaging system, determine the number of fluorophores in individual nucleating clusters, and assess RAD-51 cluster growth (Figures S5E and S5F). In accordance with a power-law fit, most RAD-51^f clusters are dimeric (Figure S5G). Inclusion of RFS-1/RIP-1(A647) shifts the cluster population toward smaller species with the monomer fraction corresponding to ~50% of the molecules. These data remain consistent with our power-law fit, $k_{obs} = J[RAD-51]^n$, where $n = 1.6$, indicating monomers, in addition to dimers, represent the substantial fraction of minimal nucleating units. Consistent with RFS-1/RIP-1(A647) stabilizing RAD-51^f on ssDNA, we observe more-frequent growth in the number of RAD-51^f protomers in individual clusters (Figure 4H). The increased frequency of RAD-51^f cluster growth provides an explanation for the stimulation of filament growth rates observed with RFS-1/RIP-1. Under the same buffer and protein-concentration used in single-molecule assays, electron microscopy analysis revealed that the inclusion of RFS-1/RIP-1 leads to enhanced RAD-51 filament formation when compared with RAD-51 alone (Figure 4I). We propose that transient engagement of RFS-1/RIP-1 with RAD-51 filaments shuts down RAD-51 dissociation events at filament ends and shifts protomer addition-dissociation equilibrium toward higher net filament-growth rates.

ATP hydrolysis regulates transient engagement of RFS-1/RIP-1 with 5' filament ends

We hypothesized that the short dwell-times of RFS-1/RIP-1 might result from ATP hydrolysis by RFS-1 or RAD-51, given

that ATP hydrolysis releases Rad51 from DNA (Chi et al., 2006; Gataulin et al., 2018; Robertson et al., 2009). Indeed, upon inclusion of the slowly hydrolysable ATP analog, ATP- γ -S, the dwell-time of RFS-1/RIP-1(A647) increased in “dipping” experiments (Figures S6A–S6C), indicating that ATP hydrolysis is at least partially responsible for RFS-1/RIP-1(A647) dissociation from RAD-51 filaments.

Next, we performed real-time imaging of RFS-1/RIP-1(A647) association with RPA-eGFP-coated ssDNA in the presence of RAD-51 and ATP (Figures 5A and 5B). Individual RFS-1/RIP-1(A647) molecules display very short dwell times on ssDNA with ATP (median, 11.3 s, 9.5–15.8 s, 96% CI; Figure 5A), similar to the dwell times observed using the dipping protocol described above. Upon inclusion of ATP- γ -S, the dwell time of RFS-1/RIP-1(A647) increased (median, 28.3 s; 22–56.2 s, 97.6% CI; Figure 5A). Notably, dwelling RFS-1/RIP-1(A647) molecules are frequently (71% of events scored, $n = 26$) located at the border of RPA-eGFP (blue) and RAD-51 filaments (dark; Figure 5B). This corroborates our previous negative-stain electron microscopy (EM) data (Taylor et al., 2015) that RFS-1/RIP-1 engages with 5' filament ends (Taylor et al., 2016) but not within RAD-51 filaments. It should be noted that we found only a few (~11%) RFS-1/RIP-1(A647) binding events associated with RAD-51-free RPA-eGFP-coated (blue) ssDNA spots. These data further support the notion that RFS-1/RIP-1 does not displace RPA on its own, but rather recognizes DNA-bound nascent RAD-51 filaments. Consistently, almost no RFS-1/RIP-1(A647) binding events are observed on RPA-eGFP-coated ssDNA when RAD-51 is absent from the assembly reaction (Figure S6D).

We have established that RAD-51 filaments grow preferentially in the 3' to 5' direction in the presence of RFS-1/RIP-1. We have also shown that RFS-1/RIP-1 shuts down dissociation of RAD-51 clusters on ssDNA leading to increased dwell times and growth frequencies. This prompted us to investigate whether labeled RFS-1/RIP-1 directly binds to 5' filament ends using gapped DNA substrates with defined polarity. To directly visualize RFS-1/RIP-1 at filament ends, we incubated RAD-51 filaments with 100 nM RFS-1/RIP-1(A647) (Figure 5C), which revealed proximity to 5', but not 3', RAD-51 filament ends (Figures 5D and 5E). Collectively, these data confirm RFS-1/RIP-1 transiently binds 5' filament ends and shuts down RAD-51 dissociation to allow for efficient filament growth in a 3' to 5' direction.

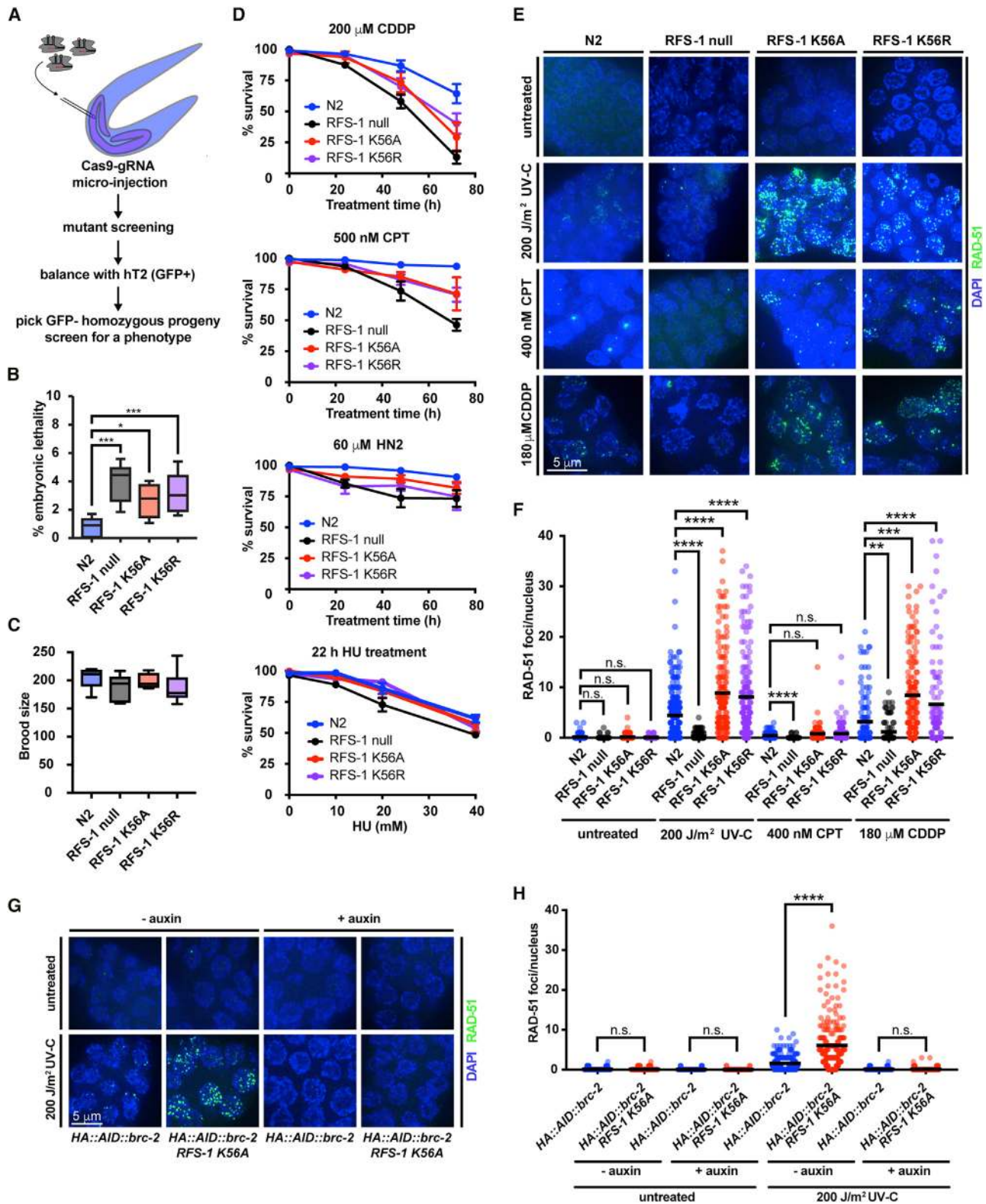
To determine whether the putative ATPase activity of RFS-1/RIP-1 is critical for the dissociation from RAD-51 filament ends, we performed dipping experiments using Alexa 647-labeled RFS-1 K56A/RIP-1 complex, in which the lysine residue

(E) Quantification of filament 5' or 3' end binding frequencies by RFS-1/RIP-1(A647) ($n = 13$ binding events). Remainder of RFS-1/RIP-1(A647) binding events observed in the experiment was binding to “dark” RAD-51 filaments forming on extended dsDNA portion of the gapped molecule. No binding of RFS-1/RIP-1(A647) to RAD-51-free RPA-eGFP-coated ssDNA was observed.

(F) Representative fluorescence images taken after RAD-51^f+RFS-1/RIP-1(A647) or RAD-51^f+RFS-1 K56A/RIP-1(A647) incubation-detection cycles with the same ssDNA construct; cumulative incubation time is indicated. RAD-51^f signal shown in blue. RFS-1/RIP-1(A647) signal shown in red.

(G) Histograms of dwell times of WT RFS-1/RIP-1(A647) ($n = 19$ clusters; top) or RFS-1 K56A/RIP-1(A647) ($n = 31$ clusters; bottom) in the presence of RAD-51^f. Number of dwell-time categories was adjusted to accommodate lower stability of bare ssDNA in the presence of RFS-1 K56A/RIP-1(A647).

(H) Histograms of dwell times of RAD-51^f alone ($n = 160$ clusters; left) or in the presence of RFS-1/RIP-1(A647) WT ($n = 57$ clusters; middle), or dwell times of RAD-51^f in the presence of RFS-1 K56A/RIP-1(A647) ($n = 49$ clusters; right).



(legend on next page)

of the Walker A box of RFS-1 is mutated to alanine. Mutating lysine to alanine/arginine in recombinase Walker A motif was previously shown to lead to abolishment of ATP binding/hydrolysis *in vitro* (Chi et al., 2006). Strikingly, RFS-1 K56A/RIP-1(A647) displays dramatically increased dwell times on RAD-51 ssDNA clusters when compared with WT RFS-1/RIP-1(A647) in the presence of ATP (Figures 5F and 5G). Notably, RFS-1 K56A/RIP-1(A647) retains the ability to stabilize RAD-51¹ clusters on ssDNA (Figure 5H), which we attribute to its ability to bind RAD-51 clusters. Inclusion of RFS-1 K56A/RIP-1 also stimulates RAD-51 assembly on RPA-eGFP-coated ssDNA in the presence of ATP, albeit less efficiently than WT RFS-1/RIP-1 (Figures S7A and 7B). When compared to WT RFS-1/RIP-1, RAD-51 filaments display slower growth rates in the presence of RFS-1 K56A/RIP-1 (Figure S7C). These observations indicate that the RFS-1 K56A/RIP-1 mutant is effective at filament end-binding and stabilization of nucleating RAD-51 clusters but is compromised for its ability to stimulate RAD-51 filament growth. Notably, increasing WT RFS-1/RIP-1 concentrations to near stoichiometric levels with RAD-51 compromises filament assembly and hinders RAD-51 filament growth when compared with the growth stimulation observed with sub-stoichiometric levels of WT RFS-1/RIP-1 (Figures S7A–S7C). This suggests that excessive filament end binding at high concentrations of RFS-1/RIP-1 or Walker A box mutants in RFS-1 blocks further recruitment of RAD-51 protomers and hinders filament elongation.

We also verified filament end binding by RFS-1 K56A/RIP-1 on filaments formed by Cy3-labeled RAD-51 (RAD-51^{Cy3}; Figures S7D and S7E). The increased dwell-times of the RFS-1 K56A/RIP-1 mutant on RAD-51 filaments are also in agreement with yeast two hybrid analysis where a robust interaction is detectable between RFS-1 K56A/RIP-1 mutant and RAD-51 but not between WT RFS-1/RIP-1 and RAD-51 (Figure S7F). Furthermore, RFS-1 K56A/RIP-1 and RFS-1 K56R/RIP-1 both form a super-shifted complex with RAD-51-ssDNA in bulk EMSA as RIP-1 does not/RIP-1 does not (Figure S7G). Collectively, these results indicate that WT RFS-1/RIP-1 engages transiently with RAD-51 filaments, whereas the greater residence time of RFS-1 K56A/RIP-1 on RAD-51 filament ends results in the formation of aberrant co-complexes, which hinder filament growth (Figure S7C).

RFS-1 K56A/R variants are competent for RAD-51 stabilization but inefficient for HR *in vivo*

To determine whether the dynamic engagement of RFS-1/RIP-1 during RAD-51 filament growth has an important role in HR *in vivo*, we generated nematode knockin mutant strains for both RFS-1 K56A and RFS-1 K56R using the CRISPR-Cas9 system (Figure 6A). Similar to the *rfs-1* (null) deletion strain, *rfs-1* K56A and *rfs-1* K56R mutant strains display a modest increase in the levels of embryonic lethality compared with the N2 (WT) strain without significant brood-size reduction (Figures 6B and 6C). In agreement with previous reports (Taylor et al., 2015; Ward et al., 2007), the *rfs-1*-null strain displays sensitivity to agents that induce replication fork breakage (Ward et al., 2007). Similarly, *rfs-1* K56A and K56R Walker A mutants are sensitive to cisplatin (CDDP), camptothecin (CPT), and nitrogen mustard (HN2), although to a lesser extent than *rfs-1*-null animals are. Sensitivity to hydroxyurea (HU) is not observed in the *rfs-1* K56A and *rfs-1* K56R mutant strains (Figure 6D).

Mitotic zones of extruded germlines were then examined for RAD-51 focus formation before and after CDDP, UV-C, and CPT treatment. In agreement with previous studies (Ward et al., 2007), RAD-51 forms damage-induced foci in N2 (WT) strains but not in the *rfs-1*-null strain. Strikingly, *rfs-1* K56A and K56R Walker A mutant strains display extensive accumulation of RAD-51 foci in response to DNA damage (Figures 6E and 6F), which persist into meiosis I. These data, together with DNA damage sensitivity, indicate that RAD-51 nucleates and is stabilized on DNA in the *rfs-1* K56A and *rfs-1* K56R mutant strains, but the resulting RAD-51 species are non-functional for repair of DNA damage via HR.

Because the RFS-1 mutants inefficiently disengage from filament ends *in vitro*, we considered the possibility that failure to efficiently disassembly from 5' filament ends may result in short, but stable, filaments unable to efficiently perform DNA strand exchange. Under these conditions, BRC-2 may continue loading RAD-51 on over-resected DNA (Symington, 2016) leading to the observed phenotype. Consistent with that possibility, the extensive accumulation of RAD-51 complexes in treated germlines of *rfs-1* K56A mutants is abolished by depletion of BRC-2 (Figures 6G and 6H). Hence, BRC-2 promotes RAD-51 nucleation on RPA-coated ssDNA and RFS-1/RIP-1 acts downstream

Figure 6. RFS-1 K56A/R *C. elegans* strains accumulate HR-incompetent RAD-51 foci after DNA damage

- (A) A schematic for CRISPR-Cas9 knockin strategy for generation of RFS-1 Walker box mutant strains.
- (B) Embryonic lethality analysis of *rfs-1* mutants *in vivo*. Percentage of unhatched eggs was scored after 24 h in strains of the indicated genotype. Progeny of 6–8 worms were evaluated.
- (C) Brood size of strains of the indicated genotype. Progeny of 5–8 worms was evaluated.
- (D) The indicated strains were treated with indicated doses of genotoxins for the indicated time. *rfs-1* null, *rfs-1* K56A and *rfs-1* K56R strains display increased sensitivity to replication-associated DSBs lesions caused by CDDP, CPT, and HN2 mustards, whereas sensitivity to replication fork stalling in the presence of hydroxyurea is mild in *rfs-1*-null strain and absent in RFS-1 K56A and RFS-1 K56R strains. Error bars represent SEM.
- (E) Representative images of the mitotic compartment of *C. elegans* germline after treatment with different genotoxins. DAPI staining (blue), RAD-51 staining (green). Scale bar represents 5 μ m.
- (F) Quantification of RAD-51 focus formation in the mitotic zone of the worm germline under different treatments in strains of the indicated genotype. Between 99 and 261 cells were quantified for each condition in 2–3 representative germlines for each genotype. Mann-Whitney test was used for statistical analysis.
- (G) Representative images of the mitotic compartment of *C. elegans* germline of indicated genotypes after treatment with indicated dose of UVC grown in the presence or absence of auxin. HA::AID::brc-2 corresponds to *C. elegans* strain modified to express BRC-2 N-terminally fused to HA followed by auxin-inducible degron. DAPI staining (blue), RAD-51 staining (green). Scale bar represents 5 μ m.
- (H) Quantification of RAD-51 focus formation in the mitotic zone of the worm germline under different treatments in strains of the indicated genotype. Between 99 and 261 cells were quantified for each condition in three representative germlines for each genotype.

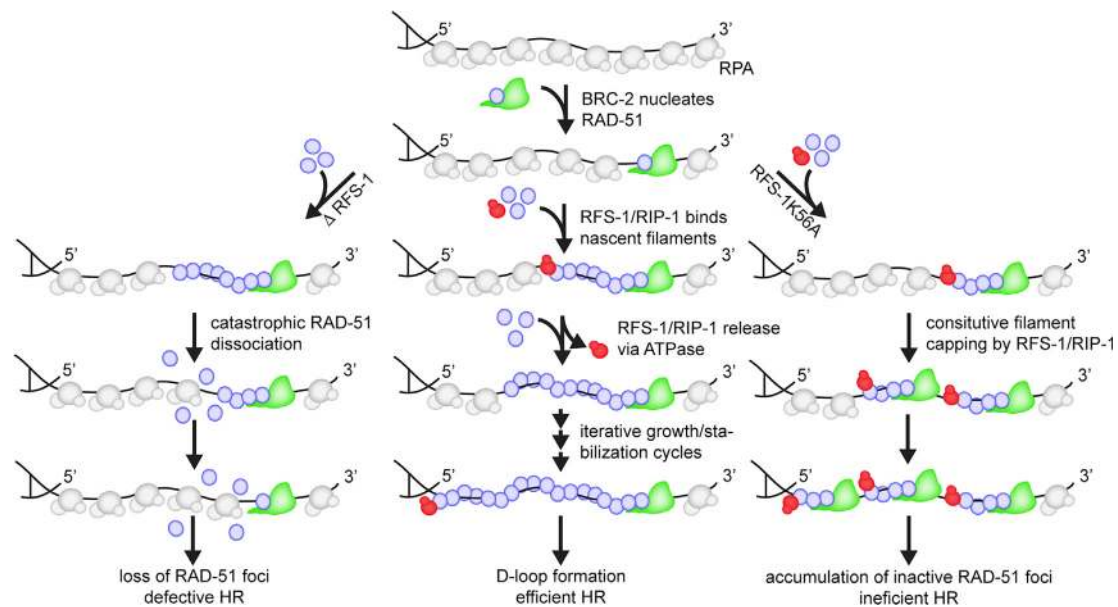


Figure 7. Model describing the mechanism of metazoan RAD-51 presynaptic filament assembly

BRC-2 nucleates RAD-51 on RPA-coated resected ssDNA. Nascent RAD-51 filaments are bound at 5' end by RFS-1/RIP-1, which stabilizes growing RAD-51 filaments preventing burst-like disassembly from filament ends. ATPase-mediated dissociation of RFS-1/RIP-1 allows for further recruitment of RAD-51 protomers allowing filament growth in 5' direction. Inability of RFS-1 K56A/RIP-1 to dissociate from bound RAD-51 filaments results in extensive end capping and formation of very stable, shorter, less-active RAD-51 filaments, which accumulate by the action of BRC-2-mediated RAD-51 nucleation.

to stabilize and facilitate growth of nascent RAD-51 filaments *in vivo*, as observed in our single-molecule experiments.

In summary, our single-molecule and genetic data support a model in which BRC-2 facilitates RAD-51 nucleation on RPA-coated ssDNA, with the recruitment of RAD-51 protomers in equilibrium with disassembly bursts from nascent RAD-51 filament ends. To shift the equilibrium in favor of filament growth, RFS-1/RIP-1 functions sequentially as a molecular chaperone by transiently binding RAD-51 filaments and preventing RAD-51 dissociation from 5' filament ends, leading to stabilization of RAD-51 on RPA-coated ssDNA. Subsequent release of RFS-1/RIP-1, which depends on ATP hydrolysis and the Walker box in RFS-1, allows for further addition of RAD-51 protomers at 5' filament end leading to the formation of a RAD-51 ssDNA filament proficient for strand exchange (Figure 7).

DISCUSSION

Here, we establish the mechanism of eukaryotic Rad51 filament nucleation and growth, which requires the sequential action of mediator proteins. We implicate BRC-2 primarily as a nucleation factor that promotes RAD-51 accumulation on RPA-coated ssDNA. In contrast to RecA, eukaryotic Rad51 nuclei grow very slowly alone. However, inclusion of the Rad51 paralog complex RFS-1/RIP-1 promotes rapid growth of RAD-51 filaments in a 3'→5' direction. This filament growth stimulation requires highly dynamic 5' filament end binding by RFS-1/RIP-1, which is regulated by intrinsic ATP hydrolysis. Hence, RFS-1/RIP-1 acts as a classical chaperone, mediating the growth of functional RAD-51 filaments *in vitro* and *in vivo*.

Division of labor between mediator proteins

Our single-molecule data reveal the contribution of mediator proteins to nucleation and growth of RAD-51 filaments. The division of labor between BRC-2 and RFS-1/RIP-1 likely stems from their intrinsic biochemical properties: BRC-2 possesses high affinity for both ssDNA and RAD-51 in solution (Martin et al., 2005; Petalcorin et al., 2006); whereas RFS-1/RIP-1 displays very low affinity for ssDNA and only interacts with RAD-51 when bound to ssDNA (Taylor et al., 2015). This is consistent with RFS-1/RIP-1 acting on RAD-51 filaments and is in agreement with multiple cellular studies showing Rad51 paralogs act downstream of BRCA2 (Chun et al., 2013; Jensen et al., 2013). Consistent with that notion, recruitment of yeast (Lisby et al., 2004) and vertebrate (Räschle et al., 2015) Rad51 paralogs (Rad55-Rad57) to DSBs is Rad51 dependent, whereas the DNA damage-dependent nematode BRC-2 foci accumulate independently of RAD-51 (Martin et al., 2005). In line with cellular data, *in vitro* studies have shown that inclusion of full-length human BRCA2 increases the number of RAD51 filaments, but not their length (Shahid et al., 2014), whereas, addition of budding yeast Rad51 paralogs Rad55-Rad57 increases the length of Rad51 filaments in negative-stain EM (Liu et al., 2011). Hence, our findings, supported by previous observations, establish that BRCA2 acts first to promote nucleation, followed by Rad51 paralogs, acting on ssDNA-bound Rad51 to promote filament growth.

Interestingly, the division of labor between BRC-2 and RAD-51 paralogs is not absolute because BRC-2 also stimulates RAD-51 filament growth, albeit to a much lesser extent than RFS-1/RIP-1 does. It remains to be tested whether interactions of BRCA2 with other HR factors (e.g., PALB2 or DSS1) might further stimulate

filament growth enhancement by BRCA2, particularly given that both PALB2 and DSS1 enhance the stimulatory effect of BRCA2 in bulk DNA strand exchange assays (Buisson et al., 2010; Zhao et al., 2015). Rad51 paralogs also appear to enhance RAD-51 nucleation rates, although this is likely due to stabilization of small RAD-51 clusters on ssDNA, rather than through direct nucleation.

Directionality of RAD-51 filament growth

Bacterial RecA filaments were previously shown to grow bi-directionally with a 2-fold kinetic preference for the 5' → 3' direction (Bell et al., 2012). Using asymmetrically positioned, gapped DNA substrates, we have shown that, contrary to RecA, nematode RAD-51 filaments grow very slowly in both directions. Strikingly, addition of RFS-1/RIP-1 specifically increases growth rates in a 3' → 5' direction, opposite to RecA. Given that human BRCA2 recognizes the 3' filament interface (Pellegriani et al., 2002) and full-length human BRCA2 binds at the 3' filament end (Shahid et al., 2014), we propose that after RAD-51 nucleation by BRC-2, the free 5' end is engaged and stabilized by RFS-1/RIP-1, allowing nascent RAD-51 filaments to be extended in a 3' → 5' direction. Furthermore, engagement of opposing ends of the filament by recombination mediators also allows for efficient cooperation during filament assembly, potentially explaining the observed synergy between BRC-2 and RFS-1/RIP-1.

Rad51 paralogs chaperone Rad51 filament growth

Previous work using bulk EM imaging postulated that Rad51 paralogs stabilize Rad51 filaments by stably intercalating into them (Liu et al., 2011). In contrast, direct single-molecule imaging revealed that RFS-1/RIP-1 engages with 5' RAD-51 filament ends in a highly dynamic manner. The 5' filament end binding is in line with predictions from previous bulk experiments (Taylor et al., 2016). Modulating RAD-51 through filament ends explains the requirement for sub-stoichiometric RFS-1/RIP-1 concentrations for RAD-51 assembly rate stimulation in bulk assays (Taylor et al., 2015). Previous work has established that disassembly from the Rad51 filament ends occurs by catastrophic dissociation bursts involving multiple Rad51 protomers (van Mameren et al., 2009). A similar phenomenon was observed in our dipping experiments. In contrast, recombinase filaments grow slowly where monomer addition is rate limiting (Bell et al., 2012; Joo et al., 2006). Suppressing costly dissociation bursts, as observed in the dipping experiments, would make an effective regulatory mechanism to stimulate net RAD-51 filament growth or to stabilize short, unstable RAD-51 clusters.

We further establish that this rapid turnover is dependent on ATPase activity of RFS-1 and demonstrate that RFS-1 Walker box mutations or blocking ATP hydrolysis stabilizes RAD-51 on ssDNA, but failure to disengage RFS-1/RIP-1 from 5' filament ends hinders further filament growth. Taken together, our results suggest that RFS-1/RIP-1 acts as RAD-51 filament chaperone by recognizing the nascent 5' RAD-51 filament ends, transiently binding them to prevent filament disassembly, and dissociating to permit further Rad51 protomer addition and filament growth. Iterative cycles allow for efficient filament extension similar to how classical molecular chaperones mediate unfolded protein recognition, folding, and release cycles.

This model is consistent with our phenotype analysis of *rfs-1*-null and Walker A box K56A/R mutant strains. Loss of RFS-1 in the null strain confers marked sensitivity to DNA damaging agents accompanied by the loss of RAD-51 foci. Strikingly, in *rfs-1* Walker A box K56A/R knockin strains, DNA damage sensitivity is also observed, but RAD-51 foci extensively accumulate, indicative of stabilized, but HR-incompetent, RAD-51 complexes. Extensive RAD-51 foci observed in *rfs-1* K56A/R background may result from continued resection and RAD-51 loading by BRC-2 as perturbations of downstream HR are known to increase resection tract length (Chung et al., 2010; Haas et al., 2018; Symington, 2016). Consistently, BRC-2 depletion abolishes the accumulation of RAD-51 foci in *rfs-1* K56A/R mutant strain, demonstrating that BRC-2 functions before RFS-1/RIP-1 *in vivo*.

Collectively, our findings contrast previous models that postulated that Rad51 paralogs intercalate and stably associate with Rad51 filaments (Liu et al., 2011) and thereby act as roadblocks for filament disruption by the anti-recombinase Srs2 helicase. Our model is corroborated in an accompanying paper by Roy et al., showing that yeast Rad55-Rad57 also exhibits highly dynamic engagement with DNA-bound Rad51 complexes during filament formation on ssDNA curtains and that depends on ATP hydrolysis. Further support to a chaperone model of Rad51 paralog action is evident from direct imaging of Srs2 performed in that same study, which revealed eviction of residual Rad55-Rad57 bypassing Srs2 molecules without any direct reduction in velocity, thereby disproving the roadblock model. In contrast, Rad55-Rad57 stimulates Rad51 filament formation behind translocating Srs2 molecules in the presence of free Rad51.

The notion that Rad51 paralogs are not stable components of Rad51 complexes is further supported by work in Chinese hamster ovary cells, in which different Rad51 paralogs were shown to turn over rapidly from the sites of replication upon challenge with genotoxic agents, whereas Rad51 persists at those sites significantly longer (Somyajit et al., 2015). Walker A box mutants of different Rad51 paralogs significantly decreased the turnover of these proteins. A similar behavior has been proposed for full-length human BRCA2 *in vitro* (Shahid et al., 2014). Together with our findings, these observations imply that mediator proteins may act as transient Rad51 filament binding factors to promote efficient Rad51 filament assembly without stable association with it.

HR and replication fork protection *in vivo*

Loss of Rad51 (Hashimoto et al., 2010), BRCA2 (Schlacher et al., 2011) and, more recently, Rad51 paralogs (Somyajit et al., 2015) has been shown to induce Mre11-dependent degradation of stalled replication forks (Hashimoto et al., 2010). Human RAD51 K133R forms very stable (Chi et al., 2006), albeit HR-incompetent, filaments (Stark et al., 2004). Expression of this mutant can suppress fork-degradation phenotypes observed in BRCA2-deficient cells, suggesting a genetic separation from HR (Schlacher et al., 2011). Notably, RFS-1- and RIP-1-deficient nematode strains display strong phenotypes in response to replication fork-blocking lesions, but not in ionizing radiation (IR)-induced DNA breaks or meiotic recombination (Ward et al., 2007). Interestingly, although RFS-1 loss sensitizes nematodes to CDDP, CPT, and HU, *rfs-1* K56A/R strains are sensitive to

CDDP and CPT, whereas, in response to HU, almost a full rescue is observed. This might imply that, similar to Rad51 K133R, RAD-51 filaments constitutively bound and stabilized by RFS-1 K56A/R are still capable of supporting fork protection but are defective for conventional HR repair of CPT- and CDDP-induced DSBs.

In conclusion, the work presented here, together with the accompanying study by Roy et al., reveals a highly conserved mechanism of Rad51 filament assembly through the action of filament chaperones.

Limitations of study

The limited spatial resolution of the system (100 nm pixel size) means that it is possible multiple RAD-51 nucleation events can occur within a single pixel. This would influence overall nucleation and growth rates as discussed. Given our reductionist approach, other components of RAD-51 assembly reaction have not been studied, such as accessory RAD-51-binding factors or posttranslational modifications, which could also influence the overall results. Finally, findings with nematode proteins might not be fully applicable to the human system, where the recombinase-ssDNA assembly mechanism might differ to a certain extent.

STAR★METHODS

Detailed methods are provided in the online version of this paper and include the following:

- **KEY RESOURCES TABLE**
- **RESOURCE AVAILABILITY**
 - Lead contact
 - Materials availability
 - Data and code availability
- **EXPERIMENTAL MODEL AND SUBJECT DETAILS**
 - Bacterial strains
 - Yeast strains
 - Nematode strains
- **METHOD DETAILS**
 - Protein expression, purification, and yeast two-hybrid interaction assays
 - Fluorescent labeling of RAD-51 and RFS-1/RIP-1
 - Single molecule imaging using dual optical trapping system
 - Single-step photobleaching and image analysis
 - EMSA
 - D-loop formation assay
 - Oligonucleotide-based DNA strand exchange assay
 - Negative stain electron microscopy
 - Genome editing using CRISPR-Cas9 in *C. elegans*
 - Injection mix for CRISPR-Cas9 editing
 - Auxin-inducible protein degradation
 - Treatment of *C. elegans* with genotoxic agents
 - Immunostaining and image acquisition
- **QUANTIFICATION AND STATISTICAL ANALYSIS**

SUPPLEMENTAL INFORMATION

Supplemental Information can be found online at <https://doi.org/10.1016/j.molcel.2020.12.020>.

ACKNOWLEDGMENTS

We thank members of Boulton, Rueda, and Martinez-Perez laboratories for discussion and critical reading of the manuscript. We thank Dr. Eric Liang and Dr. Martin Taylor for providing unlabelled RPA, Dr. Mauro Modesti for providing RPA-eGFP, and Dr. Meindert Lamers for providing Sfp expression plasmid. We thank Dr. Lumir Krejci for providing pET-MBP-1a expression vector. We thank Adam Cawte for assistance with single-step photobleaching analysis. We thank the Crick Fermentation team for help with protein expression. The work in the Boulton and Enchev laboratories is supported by the Francis Crick Institute, which receives its core funding from Cancer Research UK (FC0010048), the UK Medical Research Council (FC0010048), and the Wellcome Trust (FC0010048). S.J.B. also holds European Research Council (ERC) advanced investigator (TelMetab) and Wellcome Trust senior investigator grants. S.J.B. and D.S.R. are also funded by a Wellcome Trust collaborative grant (P67153). The Single Molecule Imaging Group is funded by a core grant of the MRC-London Institute of Medical Sciences (UKRI MC-A658-5TY10), and a BBSRC CASE-studentship (to M.D.N.). Work in the Martinez-Perez laboratory is supported by an MRC core-funded grant (M-A652-5PY60).

AUTHOR CONTRIBUTIONS

S.J.B, D.S.R., and O.B. conceived the study. O.B. expressed, purified, and fluorescently labeled the proteins; S.F. and N.O. synthesized and purified CoA A647 dye for protein labeling; O.B. and M.D.N. performed initial and advanced single-molecule experiments; O.B. and R.A. performed bulk biochemistry experiments; O.B., A.K., and D.R. analyzed the data; E.M. and R.I.E. performed negative-stain EM; C.B. generated CRISPR knockin strains in *C. elegans*; C.B. and O.B. performed *C. elegans* genetic experiments; and O.B., E.M.-P., D.S.R., and S.J.B. wrote the manuscript with editorial help from C.B., R.A., M.D.N., and R.I.E.

DECLARATION OF INTERESTS

S.J.B. is also scientific co-founder and VP Science Strategy at Artios Pharma Ltd., Babraham Research Campus, Cambridge, UK. The other authors declare no competing interests.

Received: August 6, 2020
Revised: November 2, 2020
Accepted: December 10, 2020
Published: January 8, 2021

REFERENCES

- Amitani, I., Liu, B., Dombrowski, C.C., Baskin, R.J., and Kowalczykowski, S.C. (2010). Watching individual proteins acting on single molecules of DNA. *Methods Enzymol.* 472, 261–291.
- Autour, A., C Y Jeng, S., D Cawte, A., Abdolhazadeh, A., Galli, A., Panchapakesan, S.S.S., Rueda, D., Ryckelynck, M., and Unrau, P.J. (2018). Fluorogenic RNA Mango aptamers for imaging small non-coding RNAs in mammalian cells. *Nat. Commun.* 9, 656.
- Bell, J.C., Plank, J.L., Dombrowski, C.C., and Kowalczykowski, S.C. (2012). Direct imaging of RecA nucleation and growth on single molecules of SSB-coated ssDNA. *Nature* 491, 274–278.
- Brouwer, I., Moschetti, T., Candelli, A., Garcin, E.B., Modesti, M., Pellegrini, L., Wuite, G.J., and Peterman, E.J. (2018). Two distinct conformational states define the interaction of human RAD51-ATP with single-stranded DNA. *EMBO J.* 37, e98162.
- Buisson, R., Dion-Côté, A.M., Coulombe, Y., Launay, H., Cai, H., Stasiak, A.Z., Stasiak, A., Xia, B., and Masson, J.Y. (2010). Cooperation of breast cancer proteins PALB2 and piccolo BRCA2 in stimulating homologous recombination. *Nat. Struct. Mol. Biol.* 17, 1247–1254.
- Candelli, A. (2013). Physical mechanisms of DNA repair: a single molecule perspective. PhD thesis, Vrije Universiteit Amsterdam.

- Candelli, A., Hoekstra, T.P., Farge, G., Gross, P., Peterman, E.J., and Wuite, G.J. (2013). A toolbox for generating single-stranded DNA in optical tweezers experiments. *Biopolymers* **99**, 611–620.
- Candelli, A., Holthausen, J.T., Depken, M., Brouwer, I., Franker, M.A., Marchetti, M., Heller, I., Bernard, S., Garcin, E.B., Modesti, M., et al. (2014). Visualization and quantification of nascent RAD51 filament formation at single-monomer resolution. *Proc. Natl. Acad. Sci. USA* **111**, 15090–15095.
- Chapman, J.R., Taylor, M.R., and Boulton, S.J. (2012). Playing the end game: DNA double-strand break repair pathway choice. *Mol. Cell* **47**, 497–510.
- Chi, P., Van Komen, S., Sehorn, M.G., Sigurdsson, S., and Sung, P. (2006). Roles of ATP binding and ATP hydrolysis in human Rad51 recombinase function. *DNA Repair (Amst.)* **5**, 381–391.
- Chun, J., Buechelmaier, E.S., and Powell, S.N. (2013). Rad51 paralogs BCDX2 and CX3 act at different stages in the BRCA1-BRCA2-dependent homologous recombination pathway. *Mol. Cell Biol.* **33**, 387–395.
- Chung, W.H., Zhu, Z., Papusha, A., Malkova, A., and Ira, G. (2010). Defective resection at DNA double-strand breaks leads to de novo telomere formation and enhances gene targeting. *PLoS Genet.* **6**, e1000948.
- Galletto, R., Amitani, I., Baskin, R.J., and Kowalczykowski, S.C. (2006). Direct observation of individual RecA filaments assembling on single DNA molecules. *Nature* **443**, 875–878.
- Gataulin, D.V., Carey, J.N., Li, J., Shah, P., Grubb, J.T., and Bishop, D.K. (2018). The ATPase activity of *E. coli* RecA prevents accumulation of toxic complexes formed by erroneous binding to undamaged double stranded DNA. *Nucleic Acids Res.* **46**, 9510–9523.
- Gutierrez-Escribano, P., Newton, M.D., Llauró, A., Huber, J., Tanasie, L., Davy, J., Aly, I., Aramayo, R., Montoya, A., Kramer, H., et al. (2019). A conserved ATP- and Scc2/4-dependent activity for cohesin in tethering DNA molecules. *Sci. Adv.* **5**, eaay6804.
- Haas, K.T., Lee, M., Esposito, A., and Venkiteswaran, A.R. (2018). Single-molecule localization microscopy reveals molecular transactions during RAD51 filament assembly at cellular DNA damage sites. *Nucleic Acids Res.* **46**, 2398–2416.
- Hashimoto, Y., Ray Chaudhuri, A., Lopes, M., and Costanzo, V. (2010). Rad51 protects nascent DNA from Mre11-dependent degradation and promotes continuous DNA synthesis. *Nat. Struct. Mol. Biol.* **17**, 1305–1311.
- Hegner, M., Smith, S.B., and Bustamante, C. (1999). Polymerization and mechanical properties of single RecA-DNA filaments. *Proc. Natl. Acad. Sci. USA* **96**, 10109–10114.
- Hilario, J., Amitani, I., Baskin, R.J., and Kowalczykowski, S.C. (2009). Direct imaging of human Rad51 nucleoprotein dynamics on individual DNA molecules. *Proc. Natl. Acad. Sci. USA* **106**, 361–368.
- Jensen, R.B., Carreira, A., and Kowalczykowski, S.C. (2010). Purified human BRCA2 stimulates RAD51-mediated recombination. *Nature* **467**, 678–683.
- Jensen, R.B., Ozes, A., Kim, T., Estep, A., and Kowalczykowski, S.C. (2013). BRCA2 is epistatic to the RAD51 paralogs in response to DNA damage. *DNA Repair (Amst.)* **12**, 306–311.
- Joo, C., McKinney, S.A., Nakamura, M., Rasnik, I., Myong, S., and Ha, T. (2006). Real-time observation of RecA filament dynamics with single monomer resolution. *Cell* **126**, 515–527.
- Kim, D.H., Lee, K.H., Kim, J.H., Ryu, G.H., Bae, S.H., Lee, B.C., Moon, K.Y., Byun, S.M., Koo, H.S., and Seo, Y.S. (2005). Enzymatic properties of the *Caenorhabditis elegans* Dna2 endonuclease/helicase and a species-specific interaction between RPA and Dna2. *Nucleic Acids Res.* **33**, 1372–1383.
- King, M.C., Marks, J.H., and Mandell, J.B.; New York Breast Cancer Study Group (2003). Breast and ovarian cancer risks due to inherited mutations in BRCA1 and BRCA2. *Science* **302**, 643–646.
- King, G.A., Burla, F., Peterman, E.J.G., and Wuite, G.J.L. (2019). Supercoiling DNA optically. *Proc. Natl. Acad. Sci. USA* **116**, 26534–26539.
- Lim, C.J., Zaug, A.J., Kim, H.J., and Cech, T.R. (2017). Reconstitution of human shelterin complexes reveals unexpected stoichiometry and dual pathways to enhance telomerase processivity. *Nat. Commun.* **8**, 1075.
- Lisby, M., Barlow, J.H., Burgess, R.C., and Rothstein, R. (2004). Choreography of the DNA damage response: spatiotemporal relationships among checkpoint and repair proteins. *Cell* **118**, 699–713.
- Liu, J., Doty, T., Gibson, B., and Heyer, W.D. (2010). Human BRCA2 protein promotes RAD51 filament formation on RPA-covered single-stranded DNA. *Nat. Struct. Mol. Biol.* **17**, 1260–1262.
- Liu, J., Renault, L., Veaute, X., Fabre, F., Stahlberg, H., and Heyer, W.D. (2011). Rad51 paralogs Rad55-Rad57 balance the antirecombinase Srs2 in Rad51 filament formation. *Nature* **479**, 245–248.
- Loveday, C., Turnbull, C., Ramsay, E., Hughes, D., Ruark, E., Frankum, J.R., Bowden, G., Kalmrzaev, B., Warren-Perry, M., Snape, K., et al.; Breast Cancer Susceptibility Collaboration (UK) (2011). Germline mutations in RAD51D confer susceptibility to ovarian cancer. *Nat. Genet.* **43**, 879–882.
- Martin, J.S., Winkelmann, N., Petalcorin, M.I., McIlwraith, M.J., and Boulton, S.J. (2005). RAD-51-dependent and -independent roles of a *Caenorhabditis elegans* BRCA2-related protein during DNA double-strand break repair. *Mol. Cell Biol.* **25**, 3127–3139.
- Meindl, A., Hellebrand, H., Wiek, C., Erven, V., Wappenschmidt, B., Niederacher, D., Freund, M., Lichtner, P., Hartmann, L., Schaal, H., et al. (2010). Germline mutations in breast and ovarian cancer pedigrees establish RAD51C as a human cancer susceptibility gene. *Nat. Genet.* **42**, 410–414.
- Newton, M.D., Taylor, B.J., Driessen, R.P.C., Roos, L., Cveticic, N., Allyjaun, S., Lenhard, B., Cuomo, M.E., and Rueda, D.S. (2019). DNA stretching induces Cas9 off-target activity. *Nat. Struct. Mol. Biol.* **26**, 185–192.
- Paix, A., Schmidt, H., and Seydoux, G. (2016). Cas9-assisted recombineering in *C. elegans*: genome editing using in vivo assembly of linear DNAs. *Nucleic Acids Res.* **44**, e128.
- Pellegrini, L., Yu, D.S., Lo, T., Anand, S., Lee, M., Blundell, T.L., and Venkiteswaran, A.R. (2002). Insights into DNA recombination from the structure of a RAD51-BRCA2 complex. *Nature* **420**, 287–293.
- Petalcorin, M.I., Sandall, J., Wigley, D.B., and Boulton, S.J. (2006). CeBRC-2 stimulates D-loop formation by RAD-51 and promotes DNA single-strand annealing. *J. Mol. Biol.* **361**, 231–242.
- Petalcorin, M.I., Galkin, V.E., Yu, X., Egelman, E.H., and Boulton, S.J. (2007). Stabilization of RAD-51-DNA filaments via an interaction domain in *Caenorhabditis elegans* BRCA2. *Proc. Natl. Acad. Sci. USA* **104**, 8299–8304.
- Räschle, M., Smeenk, G., Hansen, R.K., Temu, T., Oka, Y., Hein, M.Y., Nagaraj, N., Long, D.T., Walter, J.C., Hofmann, K., et al. (2015). DNA repair. Proteomics reveals dynamic assembly of repair complexes during bypass of DNA cross-links. *Science* **348**, 1253671.
- Robertson, R.B., Moses, D.N., Kwon, Y., Chan, P., Zhao, W., Chi, P., Klein, H., Sung, P., and Greene, E.C. (2009). Visualizing the disassembly of *S. cerevisiae* Rad51 nucleoprotein filaments. *J. Mol. Biol.* **388**, 703–720.
- Schlacher, K., Christ, N., Siaud, N., Egashira, A., Wu, H., and Jasin, M. (2011). Double-strand break repair-independent role for BRCA2 in blocking stalled replication fork degradation by MRE11. *Cell* **145**, 529–542.
- Shahid, T., Soroka, J., Kong, E., Maivert, L., McIlwraith, M.J., Pape, T., West, S.C., and Zhang, X. (2014). Structure and mechanism of action of the BRCA2 breast cancer tumor suppressor. *Nat. Struct. Mol. Biol.* **21**, 962–968.
- Sigurdsson, S., Van Komen, S., Bussen, W., Schild, D., Albala, J.S., and Sung, P. (2001). Mediator function of the human Rad51B-Rad51C complex in Rad51/RPA-catalyzed DNA strand exchange. *Genes Dev.* **15**, 3308–3318.
- Somyajit, K., Saxena, S., Babu, S., Mishra, A., and Nagaraju, G. (2015). Mammalian RAD51 paralogs protect nascent DNA at stalled forks and mediate replication restart. *Nucleic Acids Res.* **43**, 9835–9855.
- Stark, J.M., Pierce, A.J., Oh, J., Pastink, A., and Jasin, M. (2004). Genetic steps of mammalian homologous repair with distinct mutagenic consequences. *Mol. Cell Biol.* **24**, 9305–9316.
- Sternberg, S.H., Redding, S., Jinek, M., Greene, E.C., and Doudna, J.A. (2014). DNA interrogation by the CRISPR RNA-guided endonuclease Cas9. *Nature* **507**, 62–67.
- Symington, L.S. (2016). Mechanism and regulation of DNA end resection in eukaryotes. *Crit. Rev. Biochem. Mol. Biol.* **51**, 195–212.

Taylor, M.R.G., and Yeeles, J.T.P. (2018). The initial response of a eukaryotic replisome to DNA Damage. *Mol. Cell* **70**, 1067–1080.e12.

Taylor, M.R.G., Špirek, M., Chaurasiya, K.R., Ward, J.D., Carzaniga, R., Yu, X., Egelman, E.H., Collinson, L.M., Rueda, D., Krejci, L., and Boulton, S.J. (2015). Rad51 Paralogs Remodel Pre-synaptic Rad51 Filaments to Stimulate Homologous Recombination. *Cell* **162**, 271–286.

Taylor, M.R.G., Špirek, M., Jian Ma, C., Carzaniga, R., Takaki, T., Collinson, L.M., Greene, E.C., Krejci, L., and Boulton, S.J. (2016). A polar and nucleotide-dependent mechanism of action for RAD51 paralogs in rad51 filament remodeling. *Mol. Cell* **64**, 926–939.

Thorslund, T., McIlwraith, M.J., Compton, S.A., Lekomtsev, S., Petronczki, M., Griffith, J.D., and West, S.C. (2010). The breast cancer tumor suppressor BRCA2 promotes the specific targeting of RAD51 to single-stranded DNA. *Nat. Struct. Mol. Biol.* **17**, 1263–1265.

van Mameren, J., Modesti, M., Kanaar, R., Wyman, C., Peterman, E.J., and Wuite, G.J. (2009). Counting RAD51 proteins disassembling from nucleoprotein filaments under tension. *Nature* **457**, 745–748.

Ward, J.D., Barber, L.J., Petalcorin, M.I., Yanowitz, J., and Boulton, S.J. (2007). Replication blocking lesions present a unique substrate for homologous recombination. *EMBO J.* **26**, 3384–3396.

Watkins, L.P., and Yang, H. (2005). Detection of intensity change points in time-resolved single-molecule measurements. *J. Phys. Chem. B* **109**, 617–628.

Xu, J., Zhao, L., Xu, Y., Zhao, W., Sung, P., and Wang, H.W. (2017). Cryo-EM structures of human RAD51 recombinase filaments during catalysis of DNA-strand exchange. *Nat. Struct. Mol. Biol.* **24**, 40–46.

Yin, J., Lin, A.J., Golan, D.E., and Walsh, C.T. (2006). Site-specific protein labeling by Sfp phosphopantetheinyl transferase. *Nat. Protoc.* **1**, 280–285.

Zhang, L., Ward, J.D., Cheng, Z., and Dernburg, A.F. (2015). The auxin-inducible degradation (AID) system enables versatile conditional protein depletion in *C. elegans*. *Development* **142**, 4374–4384.

Zhao, W., Vaithiyalingam, S., San Filippo, J., Maranon, D.G., Jimenez-Sainz, J., Fontenay, G.V., Kwon, Y., Leung, S.G., Lu, L., Jensen, R.B., et al. (2015). Promotion of BRCA2-dependent homologous Recombination by DSS1 via RPA Targeting and DNA Mimicry. *Mol. Cell* **59**, 176–187.

STAR★METHODS

KEY RESOURCES TABLE

REAGENT or RESOURCE	SOURCE	IDENTIFIER
Antibodies		
rabbit polyclonal anti-RAD-51	Dr. Anton Gartner	N/A
Bacterial and virus strains		
<i>E. coli</i> BL21(DE3)	NEB	Cat# C2527I
<i>E. coli</i> DH5alpha	NEB	Cat# C2987H
<i>E. coli</i> (OP50)	Dr. Enrique-Martinez Perez	N/A
Chemicals, peptides, and recombinant proteins		
Albumin from bovine serum	Sigma-Aldrich	Cat# A7030
HiTrap SP FF 1 mL column	Merck	Cat# GE17-5054-01
Mono Q 5/50 GL column	Merck	Cat# GE17-5166-01
anti-FLAG M2 resin	Merck	Cat# A2220
3xFLAG peptide	Crick Peptide Chemistry STP	N/A
Ni-NTA agarose resin	QIAGEN	Cat# 30210
Amylose resin	NEB	Cat# E8021S
Streptavidin coated polystyrene particles 0.5% w/v	Spherotech	Cat# SVP-40-5
Lambda DNA	Thermo Fisher	Cat# SD0011
3,4-Dihydroxybenzoic acid	Merck	Cat# 99-50-3
Protocatechuate 3,4-dioxygenase	Merck	Cat# P8279-25UN
Creatine kinase (CK)	Roche	Cat# 10127566001
Creatine phosphate	Roche	Cat# 10621714001
5(6)-FAM, SE	Invitrogen	Cat# C1311
CoA Alexa 555 conjugate	Crick Peptide Chemistry STP	N/A
CoA Alexa 647 conjugate	Crick Peptide Chemistry STP	N/A
Cy3 Mono NHS Ester	Merck	Cat# GEPA13101
Cy3 Mono NHS Ester	Merck	Cat# GEPA13101
Ce his ₆ -MBP-BRC-2	This study	N/A
Ce RAD-51	This study	N/A
Ce RFS-1/RIP-1-3xFLAG	This study	N/A
Ce RFS-1 K56A/RIP-1-3xFLAG	This study	N/A
Ce RFS-1 K56R/RIP-1-3xFLAG	This study	N/A
Ce RFS-1/RIP-1-3xFLAG-YBBR	This study	N/A
Ce RFS-1 K56A/RIP-1-3xFLAG-YBBR	This study	N/A
his ₆ -SUMO protease	Dr. Peter Cherepanov	N/A
hRPA	Dr. M. R. G. Taylor	N/A
hRPA-eGFP	Dr. Mauro Modesti	N/A
hRPA-mCherry	Dr. Eric C. Greene	N/A
Sfp - phosphopantetheinyl transferase	This study	N/A
<i>S. p.</i> Cas9 nuclease V3	IDT	Cat# 1081059
<i>S. p.</i> Cas9 D10A nickase	IDT	Cat# 1081062
Indole-3 acetic acid	Alfa Aesar	Cat# A10556
Cis-diammineplatinum (II) dichloride	Sigma-Aldrich	Cat# P4394-250M
Hydroxyurea	Sigma-Aldrich	Cat# H8627-5G
Bis(2-chloroethyl)methylamine	Sigma-Aldrich	Cat# 122564-5G

(Continued on next page)

Continued		
REAGENT or RESOURCE	SOURCE	IDENTIFIER
(S)-(+)-Camptothecin	Sigma-Aldrich	Cat# C9911-250MG
Critical commercial assays		
QIAquick PCR Purification Kit	QIAGEN	Cat# 28104
Deposited data		
Original images with cropped areas marked	Mendeley	https://doi.org/10.17632/dggbg35tkk.1
Experimental models: organisms/strains		
<i>C. elegans rfs-1(fq127 [K56R]) III/hT2 (I;III)</i>	This study	ATG563
<i>C. elegans rfs-1(fq130 [K56A]) III/hT2 (I;III)</i>	This study	ATG567
<i>C. elegans brc-2(fq140[HA::AID::brc-2]) III; ieSi38 [Psun-1::TIR1::mRuby::sun-1 3' UTR, cb-unc-119(+)] IV</i>	This study	ATG600
<i>C. elegans brc-2 (fq140 [HA::AID::brc-2]) rfs-1 (fq130 [K56A]) III; ; ieSi38 [Psun-1::TIR1::mRuby::sun-1 3' UTR, cb-unc-119(+)] IV</i>	This study	ATG608
<i>C. elegans N2 (Bristol)</i>	This study	CB
<i>C. elegans rfs-1(ok1372) III.</i>	This study	RB1279
<i>S. cerevisiae</i> MaV103 parental strain for Y2H	This study	N/A
<i>S. cerevisiae yJF1 (W303-1a pep4::KanMx4 bar1::Hph-NT1 ade2-1 ura3-1 his3-11 trp1-1 leu2-3)</i> parental strain for protein expression	This study	N/A
Oligonucleotides		
See Table S1 for oligonucleotides	This study	N/A
Recombinant DNA		
Champion pET-SUMO-RAD-51	This study	N/A
pBluescript SK(-)	Dr. Lumir Krejci	N/A
pET-29-Sfp	Dr. Meindert Lamers	N/A
pET-MBP-1a-BRC-2	This study	N/A
pJF2.1(pRS303)-RFS-1/RIP-1-3xFLAG	This study	N/A
pJF2.1(pRS303)-RFS-1 K56A/RIP-1-3xFLAG	This study	N/A
pJF2.1(pRS303)-RFS-1/RIP-1-3xFLAG-YBBR	This study	N/A
pJF2.1(pRS303)-RFS-1 K56A/RIP-1-3xFLAG-YBBR	This study	N/A
pET-MBP-1a-BRC-2	This study	N/A
Software and algorithms		
GraphPad Prism 7	Graphpad	https://www.graphpad.com/scientific-software/prism/
IgorPro 8.0	WaveMetrics	https://www.wavemetrics.com/products/igorpro
SoftWoRx 3.0	Applied Precision	N/A
Fiji	Open source	https://imagej.net/Fiji
MATLAB R2018b (9.5.0)	MathWorks	https://uk.mathworks.com
Lumicks PyLake	Python package from Lumicks	https://lumicks-pylake.readthedocs.io/en/latest/index.html
Other		
C-trap optical trapping and confocal microscopy setup	Lumicks	N/A

RESOURCE AVAILABILITY

Lead contact

Further information and requests for resources and reagents should be directed to and will be fulfilled by the Lead Contact, Simon J. Boulton (simon.boulton@crick.ac.uk).

Materials availability

Plasmids, recombinant proteins, DNA substrates and newly generated nematode strains are available without restriction upon requests, which should be directed to the Lead Contact, Simon J Boulton (simon.boulton@crick.ac.uk).

Data and code availability

Original uncropped image data are available on Mendeley

[<https://doi.org/10.17632/dggbg35tkk.1>].

Custom-written data analysis scripts are available upon request from David S. Rueda (david.rueda@imperial.ac.uk).

EXPERIMENTAL MODEL AND SUBJECT DETAILS

Bacterial strains

DH5 α *E. coli* strain (genotype: fhuA2 Δ (argF-lacZ)U169 phoA glnV44 Φ 80 Δ (lacZ)M15 gyrA96 recA1 relA1 endA1 thi-1 hsdR17) was transformed with protein expression plasmids (KEY RESOURCE TABLE) and grown in Luria Broth at 37°C in the presence of 50 μ g/ml kanamycin. BL21(DE3) *E. coli* strain (genotype: fhuA2 [lon] ompT gal (λ DE3) [dcm] Δ hsdS; λ DE3 = λ sBamHI Δ EcoRI-B int::(lacI::PlacUV5::T7 gene1) i21 Δ nin5) was transformed with protein expression plasmids (KEY RESOURCE TABLE) and grown in Luria Broth at 37°C in the presence of 50 μ g/ml kanamycin and induced by 1 mM IPTG at 30°C for 4 h. OP50 *E. coli* strain was grown at 37°C in Luria Broth, spread on NGM agar plates and kept at 20°C.

Nematode RFS-1/RIP-1-3xFLAG complex and its variants were overexpressed from integrated pRS303 plasmid in *S. cerevisiae* *yJF1* (*W303-1a pep4::KanMx4 bar1::Hph-NT1 ade2-1 ura3-1 his3-11 trp1-1 leu2-3*) strain grown in YP + 2% raffinose and induced by the addition of 2% galactose. Nematode strains were propagated on NG agar plates seeded with *E. coli* (OP50) at 20-25°C.

Yeast strains

S. cerevisiae *yJF1* strain (genotype: *W303-1a pep4::KanMx4 bar1::Hph-NT1 ade2-1 ura3-1 his3-11 trp1-1 leu2-3*) strain had pRS303 plasmid variants (KEY RESOURCE TABLE) stably integrated into the genome and was grown at 30°C in YP media supplemented with 2% raffinose. Protein induction was done by the addition of 2% galactose for 4 h at 30°C. *S. cerevisiae* *MaV103* strain (genotype: MAT α *ade2-101 his3-D200 leu2-3,122 trp1-901 gal4D, gal80D, SPAL10::URA3, GAL1::lacZ, GAL1::HIS3@LYS2, can1R, cyh2R*) were transformed with Y2H protein expression plasmids and grown at 30°C at YPD agar plates or selection plates (either YP medium lacking leucine and tryptophan or YP medium lacking leucine, tryptophan, and histidine, supplemented with 100 mM 3-AT).

Nematode strains

Individual *C. elegans* strains used in the study: ATG563 (genotype: *rfs-1*(fq127 [K56R]) III/hT2 (I;III)), ATG567 (genotype: *rfs-1*(fq130 [K56A]) III/hT2 (I;III)), ATG600 (genotype: *brc-2*(fq140[HA::AID::brc-2]) III; *ieSi38* [P_{sun-1}::TIR1::mRuby::sun-1 3' UTR, cb-unc-119(+)] IV), ATG608 (genotype: *brc-2* (fq140 [HA::AID::brc-2]) *rfs-1* (fq130 [K56A]) III; ; *ieSi38* [P_{sun-1}::TIR1::mRuby::sun-1 3' UTR, cb-unc-119(+)] IV), RB1279 (genotype: *rfs-1*(ok1372) III) and N2 Bristol were maintained at 20°C on NG agar plates seeded with *E. coli* (OP50). Generation of new *C. elegans* strains is described in detail in [Method details](#), [STAR methods](#), and Table S1. Detailed information on treatment of nematode strains for different experiments is provided below in [Method details](#).

METHOD DETAILS

Protein expression, purification, and yeast two-hybrid interaction assays

RAD-51, RFS-1/RIP-1 complex and RPA complex were expressed and purified as described previously ([Taylor et al., 2015](#); [Taylor and Yeeles, 2018](#)). Since the small subunit of *C. elegans* RPA remains unknown ([Kim et al., 2005](#)), precluding the purification of a nematode RPA heterotrimeric complex, all eGFP-RPA displacement assays were performed with human eGFP-RPA. The substitution is justified given the lack of interaction between RPA and BRCA2 or RAD51 in solution ([Jensen et al., 2010](#)) and the established notion that RPA serves only as a competitor of RAD51 and can be replaced by bacterial SSB in bulk mediator assays ([Jensen et al., 2010](#)). Both BRCA2 ([Jensen et al., 2010](#)) and human RAD51 paralog complex ([Sigurdsson et al., 2001](#)) are also capable of stimulating strand exchange activity of RAD51 even in the absence of RPA under sub-saturating conditions. Human eGFP-RPA was a kind gift from Mauro Modesti (CRCM, Marseille). Yeast two-hybrid was performed as described previously ([Taylor et al., 2015](#)).

To bypass solubility problems, codon-optimized BRC-2 ORF was cloned into pET MBP-1a His₆-MBP-BRC-2 (referred to as BRC-2 in the manuscript) was expressed in BL21(DE3) *E. coli* strain at 17°C overnight using 0.1 mM IPTG for the induction of protein

expression. Cells were lysed in Lysis Buffer (25 mM Tris-HCl pH 7.5, 500 mM KCl, 10% glycerol, 1 mM DTT, 0.01% NP40 substitute, cOmplete EDTA-free protease inhibitor tablets (1/50 ml), cat no. 11873580001, Roche). After sonication and centrifugation at 20,000 rpm for 1h, clarified lysate was applied to Ni-NTA (nitrilotriacetic acid, QIAGEN) resin for 1.5h, washed with Lysis buffer and Lysis buffer containing 20 mM imidazole. Proteins were eluted using Elution buffer 500 (25 mM Tris-HCl pH 7.5, 300 mM KCl, 10% glycerol, 0.5 mM EDTA, 1 mM DTT, 0.01% NP40 substitute, 200 mM imidazole). Sample was then directly applied to amylose resin and allowed to be bound for 1h, amylose beads were washed with Wash buffer 300 (25 mM Tris-HCl pH 7.5, 300 mM KCl, 10% glycerol, 0.5 mM EDTA, 1 mM DTT, 0.01% NP40 substitute). Protein was eluted using Elution buffer 300 (25 mM Tris-HCl pH 7.5, 300 mM KCl, 10% glycerol, 0.5 mM EDTA, 1 mM DTT, 0.01% NP40 substitute, 30 mM maltose) and diluted two times with Elution buffer lacking KCl and maltose). Sample was then loaded onto pre-equilibrated HiTrap SP column, column was washed with 10 column volumes of Buffer A (25 mM Tris-HCl pH 7.5, 150 mM KCl, 10% glycerol, 0.5 mM EDTA, 1 mM DTT, 0.01% NP40 substitute) and eluted using linear salt gradient (0%–80%) of Buffer B (25 mM Tris-HCl pH 7.5, 1000 mM KCl, 10% glycerol, 0.5 mM EDTA, 1 mM DTT, 0.01% NP40 substitute). Fractions containing BRC-2 were pooled, concentrated, frozen, and subsequently checked for purity using SDS-PAGE. Ability of his₆-MBP-BRC-2 to stimulate RAD-51 in DNA strand exchange in sub-stoichiometric amounts was confirmed using previously established protocol (Thorslund et al., 2010) prior to single-molecule analysis. All protein concentrations were determined by Coomassie Blue staining using BSA standards for quantification.

Fluorescent labeling of RAD-51 and RFS-1/RIP-1

RAD-51 was labeled using amine-reactive FAM, Cy5 and Cy3 NHS-esters as described previously for RecA with modifications (Ami-tani et al., 2010). Briefly, protein storage buffer was exchanged using Zeba Column (0.5 mL resin, 3 KDa MWCO) for labeling buffer (50 mM K₂HPO₄/KH₂PO₄ (pH 7.0), 200 mM KCl, 0.1 mM DTT, and 25% glycerol). Dyes were diluted in dry DMSO to 50 mM. Dyes and protein were mixed to final concentration of 50 μM protein and 500 μM FAM-SE or 150 μM Cy3/Cy5-NHS. Incubation on rotary shaker at 4°C followed for 2 h 45 min (FAM-SE) or 2h (Cy5, Cy3-NHS). Reaction was terminated by the addition of Tris-HCl (pH 7.5) to a final concentration of 50 mM. Proteins were then buffer exchanged at least twice into storage buffer (50 mM Tris-HCl, pH 7.5, 300 mM KCl, 1 mM DTT, 0.01% NP40 substitute, 0.1 mM EDTA, 10% glycerol). Protein concentration was estimated by Coomassie staining and dye concentration was measured spectrophotometrically. Presence of minimum free dye concentration was assessed using SDS-PAGE on labeled proteins. Protein to dye concentration ratio was consistently 0.8–1.0.

For RFS-1/RIP-1 labeling we genetically fused ybbr tag (DSLEFIASKLA) on the C terminus of RIP-1 downstream of 3xFLAG tag, separated by GGGSGGG linker. Proteins were expressed and purified using a previously established protocol (Yin et al., 2006). The labeling followed a protocol described elsewhere (Lim et al., 2017). Plasmid for Sfp expression was a kind gift from Dr. Meindert Lamers (LUMC). Sfp transferase was expressed and purified as described previously (Yin et al., 2006). The purified protein complexes (5 μM) were then labeled with CoA-Cy3 (30 μM) using recombinant Sfp phosphopantetheinyl transferase (1 μM) in final buffer condition of 50 mM HEPES pH 7.5, 300 mM KCl, 10 mM MgCl₂, 1 mM DTT. After overnight incubation at 4 °C, the labeled protein complex was purified away from Sfp and free dye using Zeba column gel filtration system (0.5 mL resin, 50,000 MWCO). Proteins were stored in 20 mM Tris-acetate (pH 8.0), 100 mM potassium acetate, 10% glycerol, 1 mM EDTA, 0.5 mM DTT and subjected to SDS-PAGE and the fluorescent gel was scanned with a Typhoon9500 Scanner.

Single molecule imaging using dual optical trapping system

Experiments were performed using commercially available C-trap (LUMICKS) setup. Protein channels of the microfluidics chip were first passivated with BSA (0.1% w/v in PBS) and Pluronic F128 (0.5% w/v in PBS), minimum 500 μL of both flowed through prior to use. Biotinylated ssDNA precursor was prepared as described previously (Candelli et al., 2014). To generate gapped λ DNA, biotinylated hairpin oligonucleotides (Table S1) were annealed to λ dsDNA ends and ligated (King et al., 2019). S. p. Cas9 D10A nickase (IDT) bound to previously described (Sternberg et al., 2014) guide RNAs (Table S1) were subsequently used to generate targeted DNA nicks. The reaction was then stored at 4°C and directly diluted in PBS on the day of the experiment. DNA was captured between 4.5 μm SPHERO Streptavidin Coated polystyrene beads at 0.005% w/v using the laminar flow cell, stretched, and held at forces of 100 pN and higher until the strands were fully melted. The presence of ssDNA was verified by comparison to built-in freely joined chain model. For all the imaging conditions, ssDNA was held at forces between 10 and 20 pN, which corresponds roughly to 1.5-fold extension of B-form lambda dsDNA. Proteins were flown into incubation channels and bound to ssDNA by a previously described dipping protocol. Importantly, under low-coverage regime (concentrations of 10–100 nM), a constant flow was kept during the incubations to minimize concentration variations due to surface adhesion of labeled proteins. Beads and DNA were kept in PBS during the experiment, while DNA was melted in 0.5xNTM buffer (25 mM Tris-HCl pH 7.5, 50 mM NaCl, 0.5 mM MgCl₂) supplemented with 1 mM ATP, oxygen scavenging system (2.5 mM 3,4-dihydroxybenzoic acid, 250 nM protocatechuate dioxygenase) and 0.2 mg/ml BSA. Proteins were flown into the system in 1xNTM buffer (50 mM Tris-HCl pH 7.5, 100 mM NaCl, 1 mM MgCl₂) supplemented with 1 mM ATP, oxygen scavenging system (2.5 mM 3,4-dihydroxybenzoic acid, 250 nM protocatechuate dioxygenase) and 0.2 mg/ml BSA. When high protein concentrations were used (≥ 500 nM), ATP-regeneration system consisting of 20 mM phospho-creatine and 20 μg/mL creatine kinase was also added into the reaction.

For ‘dipping assays’ performed with different cofactors, controls using AMP-PNP-Mg²⁺ and ADP-aluminum fluoride-Mg²⁺ were performed in addition to ATP-γ-S. However, no RFS-1/RIP-1(A647) binding to RAD-51^f clusters was observed under these conditions. BRC-2 was also assessed on bare ssDNA in the ‘dipping assay’, however, we observed formation of extremely bright

aggregated GFP-BRC-2-ssDNA clusters on ssDNA containing numerous (> 20) molecules of BRC-2, which was not the case under physiological conditions with RPA. For confocal imaging, three excitation wavelengths were used, 488 nm for eGFP and 6-FAM, 532 nm for Cy3 and 638 nm for Cy5, with emission detected in three channels with blue filter 512/25 nm, green filter 585/75 nm and red filter 640 LP. Imaging conditions for 'dipping assay': 15% laser power, 0.1ms/pixel dwell-time, 100 nm pixel size. Imaging conditions for 'RPA-eGFP displacement assay': 2% blue laser power, 5% red laser power, 0.1ms/pixel dwell-time, 100 nm pixel size, 1.5 s inter-frame wait time.

Single-step photobleaching and image analysis

15% blue laser power was used to bleach RAD-51^f clusters in minimal imaging area to obtain sufficiently high bleaching time resolution. Scans were sectioned and stacked in Fiji using a custom-written script. Maximum likelihood estimation was used to determine each of the photobleaching steps within a maximum intensity/frame n . trace as previously described (Autour et al., 2018). The step sizes were subsequently binned and the histogram was fit to a double Gaussian equation in GraphPad Prism 7. For cluster growth analysis, individual clusters were analyzed for intensity increase in-between frames normalized to single-step intensity values. A cluster was considered as growing if the number of RAD-51^f promoters in the cluster increased by at least a single RAD-51^f promoter during the time the cluster dwelled on ssDNA. The growth frequency of RAD-51^f clusters was reported for each individual ssDNA molecule. For real-time RPA-eGFP displacement analysis, real-time force and fluorescence data were exported from BlueLake HDF5 files and analyzed using custom-written scripts in Pylake Python package. Force was down sampled to 3 Hz for plotting. For RPA-eGFP free patch edge binding analysis, custom position-analysis script was built to extract the position of individual RPA-eGFP peaks and depressions, A647 intensity peaks were then aligned and their maxima position extracted to monitor proximity to the RPA-eGFP signal depression edges. For apparent nucleation rate analysis in Figure 2E we used custom-made algorithm to quantify the Rad51 nucleation frequency from the kymograph showing eGFP-RPA displacement in time. In each kymograph, color level for the blue channel was adjusted to increase the contrast. Subsequently, the image was median-filtered in x axis (25 frames window). A negative of the image was then smoothed in y axis by the signal convolution function and subsequently the process was repeated in x axis (5 pixel window). A peak detection function was employed on the processed image to quantify the number of RAD51 filaments in time. The number of detected peaks in time was fitted with a single exponential function $y = A_{\max} (1 - \exp(-k^*t))$. Worm-like chain (WLC) model for λ dsDNA was used as a reference for force-extension curve comparison. Custom-written WLC fitting script was used to calculate contour length and subsequently gapped length of gapped DNA substrates. Growth rates in real-time experiments as well as dwell-times and binding frequencies were estimated in Fiji. Nucleation frequencies were plotted as a function of RAD-51^f concentration and fitted with power-law in GraphPad Prism 7. Dwell-times of RAD-51 clusters were binned into appropriate dwell-time categories cumulative survival analysis was performed using Igor 8.0. Mann-Whitney test was used to assess statistical significance of the data where appropriate.

EMSA

Proteins were diluted from concentrated stocks into Storage Buffer, which was also used in no protein controls. For native polyacrylamide gels, proteins were mixed with a master mix (containing 60 nM (nucleotides) 5'-[32P]-labeled 60-mer oligonucleotide (ACGCTGCCGAATTCTACCAGTGCCTTGCTAGGACATCTTTGCCACCTGCAGGTTCAACC), 20 mM Tris-HCl (pH 7.5), 8% glycerol, 1 mM DTT, 50 mM sodium acetate, 2 mM MgCl₂ and 2 mM ATP, and incubated for 10 min, before crosslinking with 0.25% glutaraldehyde for 10 min, all at 25°C. Reactions were resolved on 1% agarose gels in 1X TBE (70 V, 2 h 20 min). Gels were dried and imaged by autoradiography or using a storage phosphor screen (Amersham Biosciences) and Typhoon9500 and quantified using Fiji. For fluorescence experiments using RAD-51^f and/or labeled RFS-1/RIP-1 complex, proteins were incubated with 20 nM 49-mer oligonucleotide AGCTACCATGCCTGCACGAATTAAGCAATTCGTAATCATGGTCATAGCT in 35 mM Tris-HCl (pH 7.5), 50 mM KCl, 1 mM DTT, 2 mM MgCl₂, 2 mM ATP and incubated for 10 min at 25°C followed by resolution on 0.8% agarose gel in 1X TAE (70 V, 60 min). Gels were dried and imaged using Typhoon9500 and appropriate filter settings. % of DNA binding was assessed using Fiji.

D-loop formation assay

RAD-51 and RAD-51^f were diluted from concentrated stocks into T Buffer (25 mM Tris-HCl (pH 7.5), 10% glycerol, 0.5 mM EDTA (pH 8.0), 100 mM KCl), which were also used in no protein controls. Proteins were mixed with 30 nM Cy5-labeled 90-mer ssDNA in 35 mM Tris-HCl (pH 7.5), 50 mM KCl, 1 mM DTT, 2 mM MgCl₂ and 2 mM ATP and incubated for 10 min at 25°C followed by addition of 0.54 μ g pBS(-) dsDNA plasmid for further 15 min incubation at 25°C. Reactions were terminated by SDS-PK treatment for 10 min at 37°C. 90V/35 min resolution using 1xTAE, 0.8% agarose gel electrophoresis followed. Gels were scanned using Typhoon9500 with appropriate filter settings.

Oligonucleotide-based DNA strand exchange assay

40-mer dsDNA was prepared by annealing 5'-fluorescein-labeled 40-mer oligonucleotide (TAATACAAAATAAGTAAATGAATAAACA GAGAAAATAAAG) to the complementary unlabelled 40-mer oligonucleotide (CTTTATTTCTCTGTTTATTCATTTACTTATTTG TATTA) in 50 mM Tris-HCl (pH 7.5), 100 mM NaCl, 10 mM MgCl₂, and stored at stock concentration 200 nM (moles). Proteins were diluted from concentrated stocks into T Buffer (25 mM Tris-HCl (pH 7.5), 10% glycerol, 0.5 mM EDTA (pH 8.0), 50 mM KCl),

which was also used in no protein controls. Proteins were mixed with 5.6 nM (moles) 150-mer oligonucleotide (TCTTATTATGTCTCTTTTATTTTCATTTTCCTATATTTATTCCTATTATGTTTTATTCATTTACTTATTCTTTATGTTTCATTTTTATATCCTTTACTTTATTTCTCTGTTTATTCATTTACTTATTTGTATTATCCTTATCTTATTTA), 50 mM Tris-HCl (pH 7.5), 1 mM DTT, 100 μ g/ml of BSA, 2 mM ATP, 4 mM CaCl_2 in 12.5 μ L reaction volume at 25°C for 10 min. 0.5 μ L dsDNA stock and 0.5 μ L 0.1 M spermidine were then added incubated for 1:30 h. The samples were deproteinized with 0.1% SDS and 12.5 μ g proteinase K at 37°C and resolved in 10% polyacrylamide gels in 1X TBE (80 V, 1 h 15 min). Gels were imaged on a Typhoon9500 and quantified using Fiji.

Negative stain electron microscopy

RAD-51 and RFS-1/RIP-1 in indicated concentrations were incubated with 250 nM (in nucleotides) 150-mer poly(dT) ssDNA in 50 mM Tris-HCl, pH 7.5, 100 mM NaCl, 2 mM MgCl_2 , 2 mM ATP for 5 min °C. For negative staining, Quantifoil R2/2, 2 nm carbon, 400 Cu mesh grids were glow discharged for 30 s at 25 mA with a K100X glow discharger (EMS), 4 μ L of sample was added to the grid left for 1 min. Excess sample was blotted away leaving a thin film. Then the grid was dipped into buffer solution twice and dipped twice into 2% uranyl acetate solution, blotting in between. Negative stain EM data were acquired on Tecnai Spirit TEM operated at 120 kV, equipped with a n FEI Eagle CCD camera.

Genome editing using CRISPR-Cas9 in *C. elegans*

Genome editing by CRISPR-Cas9 was performed using preassembled Cas9-sgRNA complexes (trRNA, crRNA, Cas9) and single-stranded DNA oligos (used as repair templates) as described before (Paix et al., 2016). *dpy-10* was used as a co-injection marker to select progeny carrying Cas9-induced edits. The following sequences were used to generate crRNAs (IDT): *rfs-1* K56 mutants: TTTAGGAGTTGGTAAAACAC; *HA::AID::brc-2*: TTTTATAGATGAGTCACCCAT; *dpy-10*: GCTACCATAGGCACCACGAG. The repair templates used (Table S1) were ordered as single-stranded DNA oligos at 4 nmol (IDT).

Injection mix for CRISPR-Cas9 editing

crRNAs and trRNA were reconstituted with nuclease-free duplex buffer to 200 μ M and mixed in equal volumes to generate crRNA:trRNA duplex at 100 μ M. Cas9/crRNA/trRNA complexes were generated by adding 2 μ L of crRNA:trRNA duplex (100 μ M) of the target gene, 0.2 μ L of *dpy-10* crRNA:trRNA duplex (100 μ M), and 2.95 μ L of Cas9 nuclease V3 (at 61 μ M, #1081059, IDT) and incubating the mix at room temperature for 5 min. The final injection mix was prepared by adding 0.6 μ L of each ssDNA repair template from a 100 μ M stock and 0.5 μ L of *dpy-10* repair template (10 μ M stock) to 5.15 μ L of the Cas9/crRNA/trRNA complex, the mix was completed with H_2O to obtain a final volume of 10 μ L. The injection mix was directly injected into the gonads of young adult worms. Following injection, worms were placed onto individual NG agar plates seeded with *E. coli* (OP50) and incubated at 25°C for three days. Roller and dumpy worms, caused by Cas9-dependent editing of the *dpy-10* gene, were picked individually to plates and allowed to produce progeny that was screened by PCR for the presence of the desired edit.

Auxin-inducible protein degradation

Auxin-mediated degradation of BRC-2 in the germline was performed by creating a strain homozygous for the *ieS138* transgene, expressing *TIR-1-mRuby* under the *sun-1* promoter (Zhang et al., 2015), and for the CRISPR-generated *HA::AID::brc-2* allele. Young adult worms were placed on NG agar plates containing 4 mM auxin (Indole-3 acetic acid, Alfa Aesar, # A10556) seeded with *E. coli* (OP50) and allowed to lay eggs for 2 h. Embryos were cultured on the auxin-containing plates for three days before young adults were picked and processed for immunostaining.

Treatment of *C. elegans* with genotoxic agents

Exposure of worms to indicated doses of Cis-Diammineplatinum (II) dichloride (#P4394-250MG, Sigma, CDDP), Hydroxyurea (#H8627-5G, Sigma, HU), bis(2-chloroethyl)methylamine (122564-5G Sigma, HN2), and (S)-(+)-Camptothecin (#C9911-250MG, Sigma, CPT), was performed by placing worms on NG agar plates containing the desired amount of each genotoxic agent. Randomly picked young adult animals were placed on MYOB plates containing 200 μ M CDDP, 500 nM CPT, 60 μ M HN2 cisplatin or control plates. 3-5 worms were plated on each plate. Worms were moved every 24 h to new drug-containing plates. Embryonic survival of progeny was then determined by determining the number of hatched eggs (calculated from initial number of laid eggs and dead eggs) on the 0–24, 24–48, and 48–72 h plates. For HU treatment, worms were plated on plates containing indicated concentration of HU, for indicated period of time. Animals were transferred to HU-free plates and allowed to recover for 3 h. Worms were then allowed to lay eggs for 4 h. Dead eggs were counted 24 h after removing the parent animals.

Immunostaining and image acquisition

Randomly picked gravid adult hermaphrodites were treated with cisplatin (CDDP, 180 μ M) for 19 h and camptothecin (CPT, 500 nM) for 18 h in liquid culture ionizing irradiation and UV-C (254 nm) treatment were performed on seeded plates. UV-C treatment of worms was performed on seeded plates using BLX-254 instrument. After treatment, animals were transferred to fresh seeded plates and allowed to recover (CDDP, 18 h; CTP, 7h; UV-C, 2h). Worms were washed twice in PBS, transferred to poly-L-lysine coated slides and germlines dissected. Germlines from young adults hermaphrodites were dissected in egg buffer (118 mM NaCl, 48 mM KCl_2 , 2 mM CaCl_2 , 2 mM MgCl_2 , 5 mM HEPES at pH 7.4) and fixed in 1% paraformaldehyde containing 0.1% Tween for 5 min. Slides

were frozen in liquid nitrogen, then immersed for 1 min in methanol at -20°C and transferred to PBST (1 × PBS, 0.1% Tween). After washing the slides three times in PBST for 5 min, they were blocked in PBST 0.5% BSA for 30 min before incubating then overnight at room temperature with PBST containing anti-RAD-51 antibodies (a kind gift from A. Gartner) diluted 1:500 were incubated overnight at room temperature. Following three washes of 10 min each in PBST, slides were incubated with secondary antibodies (Alexa 488 α -rabbit, 1:500) for two h in the dark. Following three washes of 10 min each in PBST, slides were counterstained with DAPI, washed in PBST for 1 h and mounted using Vectashield. All images were acquired as stacks of optical sections with an interval of $0.2\ \mu\text{m}$ using a Delta Vision deconvolution system equipped with an Olympus 1X70 microscope using 100x lenses. Images were subjected to deconvolution using SoftWoRx 3.0 (Applied Precision).

QUANTIFICATION AND STATISTICAL ANALYSIS

Scans were sectioned and stacked in Fiji using a custom-written script. Maximum likelihood estimation was used to determine each of the photobleaching steps within a maximum intensity/frame n . trace as previously described (Autour et al., 2018). The step sizes were subsequently binned and the histogram was fit to a double Gaussian equation in GraphPad Prism. 7. For cluster growth analysis, individual clusters were analyzed for intensity increase in-between frames normalized to single-step intensity values. A cluster was considered as growing if the number of RAD-51^f promoters in the cluster increased by at least a single RAD-51^f promoter during the time the cluster dwelled on ssDNA. The growth frequency of RAD-51^f clusters was reported for each individual ssDNA molecule. For real-time RPA-eGFP displacement analysis, real-time force and fluorescence data were exported from BlueLake HDF5 files and analyzed using custom-written scripts in Pylake Python package. Force was down sampled to 3 Hz for plotting. For RPA-eGFP free patch edge binding analysis, custom position-analysis script was built to extract the position of individual RPA-eGFP peaks and depressions. A647 intensity peaks were then aligned and their maxima position extracted to monitor proximity to the RPA-eGFP signal depression edges. For apparent nucleation rate analysis in Figure 2E we used custom-made algorithm to quantify the Rad51 nucleation frequency from the kymograph showing eGFP-RPA displacement in time. In each kymograph, color level for the blue channel was adjusted to increase the contrast. Subsequently, the image was median-filtered in x axis (25 frames window). A negative of the image was then smoothed in y axis by the signal convolution function and subsequently the process was repeated in x axis (5 pixel window). A peak detection function was employed on the processed image to quantify the number of RAD51 filaments in time. The number of detected peaks in time was fitted with a single exponential function $y = A_{\text{max}}(1 - \exp(-k^*t))$. Worm-like chain (WLC) model for λ dsDNA was used as a reference for force-extension curve comparison. Custom-written WLC fitting script was used to calculate contour length and subsequently gapped length of gapped DNA substrates. Growth rates in real-time experiments as well as dwell-times and binding frequencies were estimated in Fiji. Nucleation frequencies were plotted as a function of RAD-51^f concentration and fitted with power-law in GraphPad Prism 7. Dwell-times of RAD-51 clusters were binned into appropriate dwell-time categories cumulative survival analysis was performed using Igor 8.0. Mann-Whitney or other statistical test was used to assess statistical significance of the data where appropriate – sample size and statistical significance are indicated in the figures.